nature physics

SUPPLEMENTARY INFORMATION
https://doi.org/10.1038/s41567-019-0603-8

In the format provided by the authors and unedited.

The odd free surface flows of a colloidal chiral fluid

Vishal Soni[1,8], Ephraim S. Bililign[1,8], Sofia Magkiriadou[1,7,8], Stefano Sacanna[2], Denis Bartolo[3], Michael J. Shelley[4,5] and William T. M. Irvine[6*]

[1]James Franck Institute and Department of Physics, University of Chicago, Chicago, IL, USA. [2]Molecular Design Institute, Department of Chemistry, New York University, New York, NY, USA. [3]Laboratoire de Physique, ENS de Lyon, Université de Lyon, Université Claude Bernard, CNRS, F-69342, Lyon, France. [4]Center for Computational Biology, Flatiron Institute, New York, NY, USA. [5]Courant Institute, New York University, New York, NY, USA. [6]James Franck Institute, Enrico Fermi Institute and Department of Physics, University of Chicago, Chicago, IL, USA. [7]Present address: Laboratory for Experimental Biophysics, Institute of Physics, École Polytechnique Fédérale de Lausanne (EPFL), Lausanne, Switzerland. [8]These authors contributed equally: Vishal Soni, Ephraim S. Bililign, Sofia Magkiriadou. *e-mail: wtmirvine@uchicago.edu

Supplementary Materials for

The odd free surface flows of a colloidal chiral fluid

Vishal Soni*, Ephraim S. Bililign*, Sofia Magkiriadou*, Stefano Sacanna, Denis Bartolo, Michael J. Shelley, William T. M. Irvine

Contents

1 Experimental Setup **1**
1.1 Colloidal sample 1
1.2 Magnetic field control 1
1.3 Imaging, particle tracking, and spinning-rate measurements 1

2 Experimental Procedures **2**
2.1 Roll and drift compensation 2
2.2 Control of the initial conditions 3
2.2.1 Flat strip experiments 3
2.2.2 Droplet coalescence 3
2.2.3 Droplet spreading 3
2.2.4 Bubble collapse 3
2.2.5 Flow past an obstacle 3
2.3 Interface experiments 3

3 Characterization of the spinner fluid **5**
3.1 Substrate friction 5
3.2 Velocity profile and rotational and shear viscosities 6

4 Measurement of surface wave spectrum and dissipation **9**
4.1 Fitting the dissipation 10
4.2 Disambiguating Hall viscosity and surface tension 10

5 Characterization of the strip instability **12**

6 Hydrodynamic theory of the colloidal chiral fluid **13**
6.1 Equations of motion 13
6.2 The role of magnetism 15
6.2.1 Absence of Rosensweig surface instability 16
6.3 Steady-state solutions 18
6.3.1 The semi-infinite geometry 18
6.3.2 The slab geometry 19
6.3.3 The droplet geometry 19
6.4 Perturbation of flow in a semi-infinite slab 19
6.4.1 Linearization scheme 19
6.4.2 Linear theory 20
6.4.3 Solution 20
6.4.4 Visualization and asymptotics 21

6.5 Perturbation of flow in a finite slab . . . 23
6.5.1 Linearization scheme . . . 23
6.5.2 Linear theory . . . 23
6.5.3 Solution . . . 24
6.5.4 Visualization and asymptotics . . . 25
6.6 Perturbation of droplet flow . . . 29
6.6.1 Solution and visualization . . . 29
6.7 Physical interpretation of dynamics . . . 30
6.7.1 Surface waves driven by "edge pumping" . . . 30
6.7.2 Effects of Hall stress . . . 32
6.7.3 Hall damping . . . 32
6.7.4 Capillary Hall waves . . . 33
6.7.5 Effects of finite odd substrate friction . . . 34
6.7.6 An odd hydrodynamic instability . . . 37

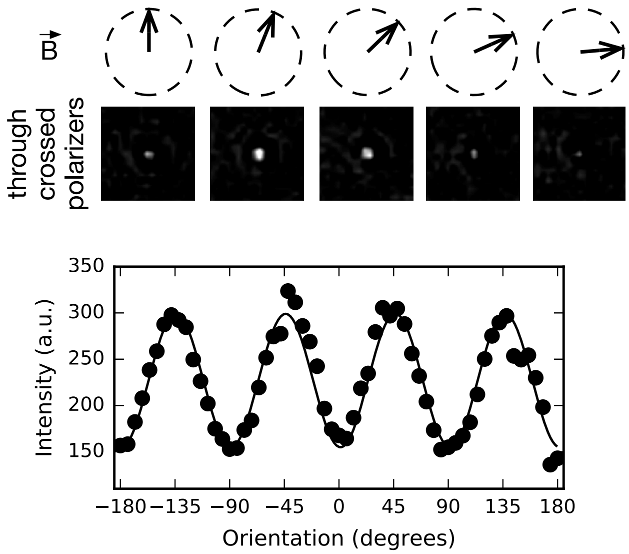

Supplementary Figure S1: **Measuring the particles' spinning frequency.** **a**, When viewed through crossed polarizers, a hematite cube blinks four times during one full rotation. This allows us to confirm that, in our experiments, the particles spin at the frequency set by the rotating magnetic field. **b**, We hold several isolated particles ($\sim$15) at fixed angles and we record their mean intensity. All particles blink four times in one full rotation of the magnetic field.

1 Experimental Setup

1.1 Colloidal sample

We synthesize hematite cubes following the method described by Sugimoto et al in [1], and subsequently coat them in a thin silica shell using a Stöber method described in [2]. We suspend the cubes in water and, unless otherwise noted, we enclose the suspension in a glass chamber (see Figure S4a).

1.2 Magnetic field control

We generate rotating magnetic fields by three pairs of coils. In all experiments we control the magnitude ($B = 1.3$ mT) and orientation of the magnetic field with a computer. We program the field parameters in a Python script and send them to a National Instruments DAQ card (PCIe-6363) via the PyDAQmx Python driver [3]. We then amplify the DAQ output voltage by a custom voltage-to-current amplifier that powers each coil pair. We record the currents through all coils continuously, so the orientation of the magnetic field at every moment in time is known.

1.3 Imaging, particle tracking, and spinning-rate measurements

We observe the individual colloidal particles and the macroscopic flows of spinner fluids either with a Nikon Eclipse TE2000-U microscope and 10x-100x objectives, or with a Zeiss Axio Zoom.V16 microscope and a 2.3x objective that allows continuous magnification from 16.1x to 258x. We record slow dynamics ($\leq$5 fps) with a color camera (Grasshopper2 GS2-GE-20S4C-C, Grasshopper3 GS3-U3-123S6C-C) and fast dynamics ($\sim$1000 fps) with a black-and-white camera (Phantom v12, Phantom v2512, Phantom VEO 640S).

As mentioned in the main text, the colloidal particles are birefringent: when imaged through crossed polarizers, their intensity depends on their orientation. In particular, they blink four times during one full rotation as illustrated in Figure S1 and shown in Supplementary Movie 8. Thus, by monitoring the intensity of the spinner fluid with a camera triggered in synchrony with the magnetic field, we confirm that the particles rotate at the rotating frequency of the driving magnetic field up to 15 Hz.

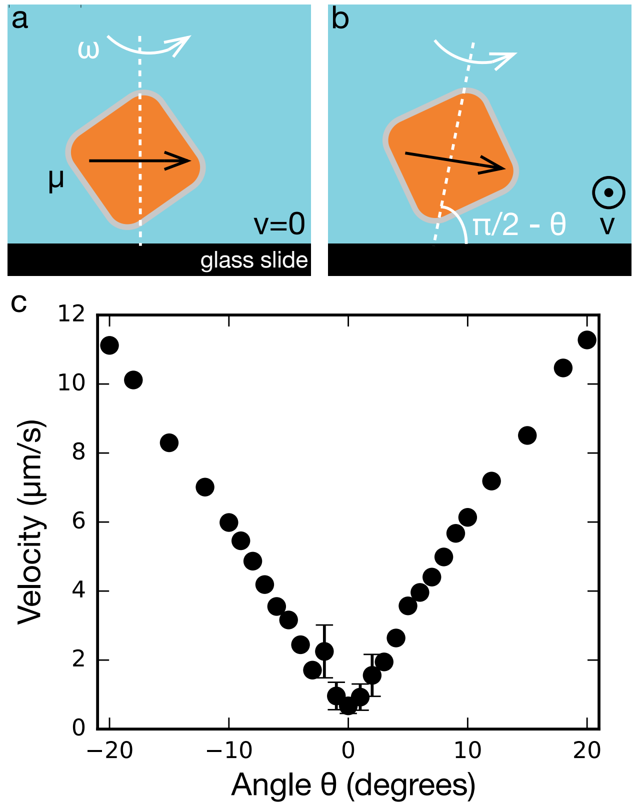

Supplementary Figure S2: **Rolling motion. a,** If the rotation axis of the magnetic field is perpendicular to the substrate, the particle spins in place without rolling. Its translational velocity vanishes, $v = 0$. **b,** If the rotation axis of the magnetic field is not perpendicular to the substrate and deviates from the normal by an angle θ, the particle will roll as it spins and $v \neq 0$. **c,** The rolling speed depends linearly on the tilt angle θ for angles at least up to 20 degrees.

After confirming that the particles rotate at the same rate Ω, we measure the instantaneous particle positions. We first average frames over one intensity oscillation, in order to avoid brightness fluctuations. We then identify particle positions and track their trajectories using the free python package trackpy [4].

2 Experimental Procedures

2.1 Roll and drift compensation

In order to observe dynamics at long timescales, care must be taken to minimize particle drift. Drift can occur either due to a tilt of the experimental setup with respect to gravity, which will cause sedimentation; or due to a misalignment of the spinning axis of the magnetic field, which will cause rolling (see Figure S2a, b). In the case of low-friction experiments, particles naturally collect in a locally flat region due to gravity, eliminating sedimentation. Meanwhile, for high-friction experiments, we minimize sedimentation by adjusting the tilt of the sample with the magnetic field off. As shown in Figure S2c, the rolling velocity is linearly proportional to the angle between the spinning axis and the normal to the substrate for a wide range of angles. We minimize rolling by adjusting the relative amplitudes of the currents through all three coil pairs until particle clusters do not move by more than a couple of pixels within a couple of minutes.

Our setup allows arbitrary control of the magnetic field axis, which enables rolling the particles in any desirable direction. This feature is very useful for the preparation of the initial state in many of our experiments.

2.2 Control of the initial conditions

2.2.1 Flat strip experiments

In experiments that require flat strips of the spinner fluid (surface waves and hydrodynamic instability, see Figures 2 and 4 in the main text and Supplementary Movies 7, 11), we prepare strips by accumulating particles against a straight edge, either by rolling all particles to one side (see Figure S2), or by tilting the sample. We control the thickness of the strips by changing the concentration of the suspension.

2.2.2 Droplet coalescence

To observe droplet coalescence, shown in Figure 1d and Supplementary Movie 3, we spin particles for a few minutes until they form small clusters; these clusters then gradually coalesce into larger ones as exemplified in Supplementary Movie 1.

2.2.3 Droplet spreading

For droplet spreading, shown in Figure 1e and Supplementary Movie 4, we cast a small amount of suspension ($\sim 2\,\mu$L) on a glass slide and seal it with a drop of UV-curable Norland Optical Adhesive (NOA 81), which creates a hard boundary around the suspension. We then spin the particles until they all assemble into a single drop. Finally, to guide the drop towards the wall, we tilt the microscope. This procedure is sketched in Figure S3a.

2.2.4 Bubble collapse

For experiments on the collapse of bubbles, illustrated in Figure 1f and Supplementary Movie 5, we enclose the suspension in a glass chamber that contains, on one wall, cured droplets of Norland Optical Adhesive (NOA 81). We guide the particles with a permanent magnet over a drop of the adhesive and then spin them until they all sediment downhill. We subsequently flip the sample upside-down, so that all particles and their void end up on the flat side of the chamber. This procedure is sketched in Figure S3b.

2.2.5 Flow past an obstacle

For experiments involving flow past an obstacle, shown in Figure 1g and Supplementary Movie 6, we use the same cured NOA 81 droplets as obstacles. We induce flow by tilting the microscope, thereby allowing the particles to sediment while spinning. This procedure is sketched in Figure S3c.

2.3 Interface experiments

Low-friction experiments are performed by placing the particles at a fluid-fluid interface between water and either oil or air. In these experiments the particles are suspended in a water mixture with 15 wt% glycerol to mediate evaporation. In addition, we add a surfactant (4 mM Sodium dodecyl sulfate , Sigma-Aldrich), to prevent the particles from breaching the interface. We pipette a small amount of the particle suspension ($\sim 0.7\,\mu$L) on a glass slide and enclose it in a glass chamber. The remainder of the chamber is either left empty (air interface experiments) or filled with pure silicone fluid (Clearco Products) of variable viscosity (oil interface experiments). The entire sample is then held such that the cubes sediment with gravity to the water/air (oil) interface. A typical sample geometry is illustrated in Figure S4b. The typical radius of curvature is $R \sim 10^5\,\mu$m. For a typical droplet of fluid $R \sim 100\,\mu$m, this amount of curvature varies the particle rotation axis by an angle $\theta \sim 0.2°$ with respect to the substrate, resulting in negligible amounts of rolling motion (see Figure S2c).

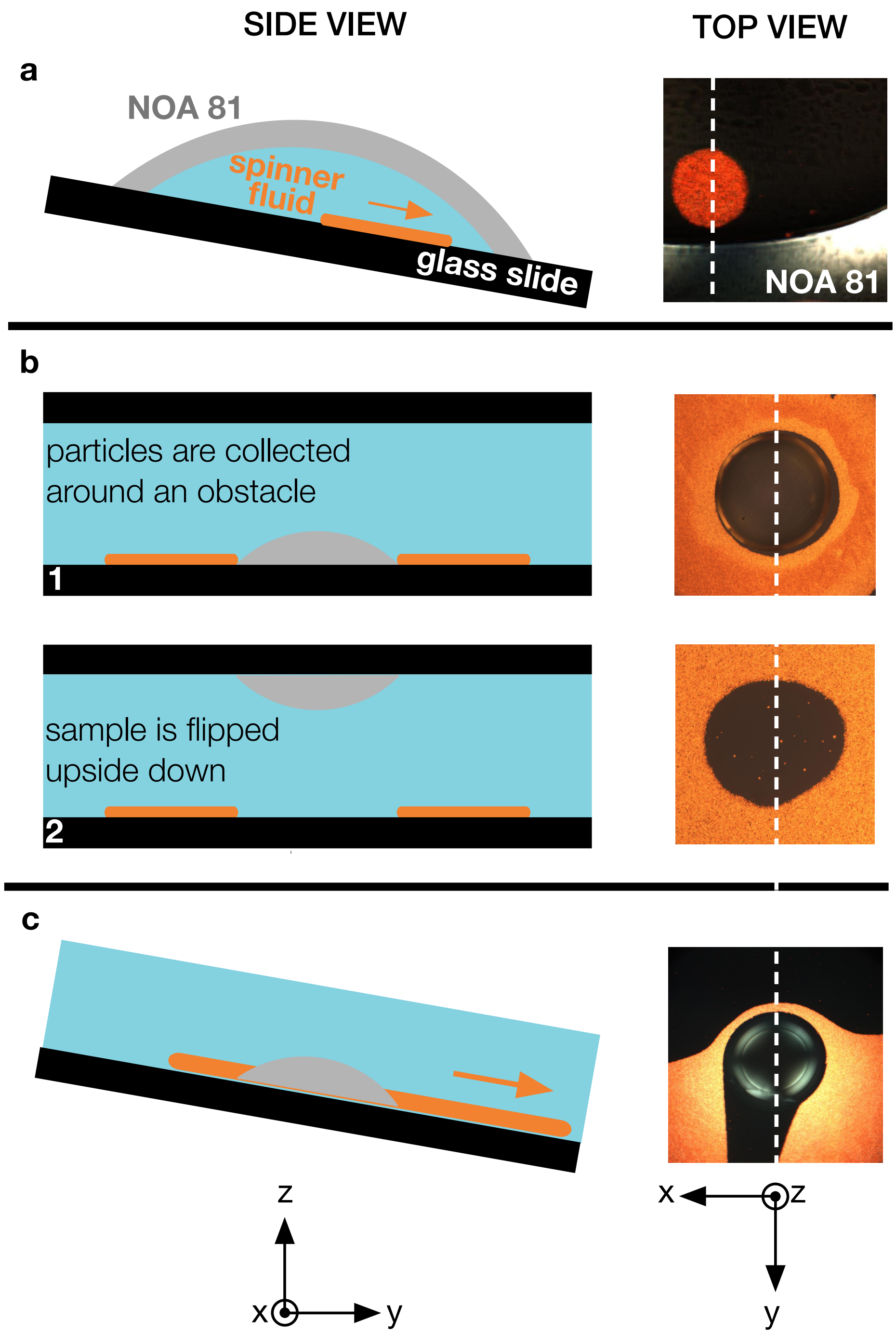

Supplementary Figure S3: **Schematic of sample preparation.** Left column: side view; right column: top view, with the white dashed line marking the cross section represented in the side view. **a**, We enclose a droplet of aqueous suspension of hematite cubes between a glass slide and a drop of UV-curable Norland Optical Adhesive (NOA 81). After the particles have come together into a single droplet of spinner fluid, we tilt the sample to drive them towards the hard wall made by the cured NOA 81. **b**, To make a hole in the spinner fluid, we put the suspension of hematite cubes in a chamber that contains a cured droplet of NOA 81 on the bottom. We collect the particles around the NOA 81 and then flip the sample upside-down. **c**, To probe the flow of the spinner fluid past obstacles, we use the same cured droplets of NOA 81 as the obstacles, and we tilt the sample to create flow via sedimentation.

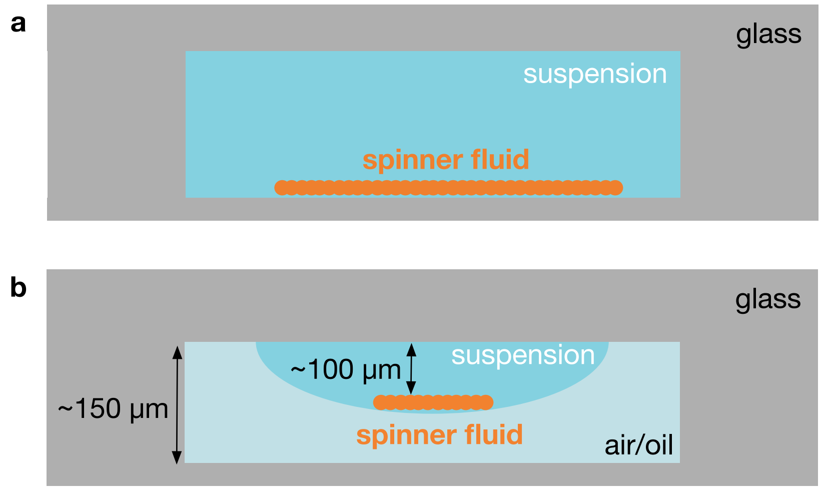

Supplementary Figure S4: **Colloids at interfaces of variable friction.** **a**, In the conventional geometry cubes are sedimented onto a glass substrate. **b**, By contrast, to achieve lower substrate friction, a droplet of colloidal suspension is enclosed in glass chamber otherwise filled with either oil or air, allowing the colloids to sediment onto a fluid-fluid interface.

3 Characterization of the spinner fluid

We deduce all of the parameters found in the hydrodynamic equations of our spinner fluid experimentally. We perform these measurements on circular droplets of spinner fluid, as shown in Figure 3 in the main text and described below.

3.1 Substrate friction

While the colloidal particles comprising our fluid spin in the vicinity of a substrate, the hydrodynamic interaction between the particles and substrate can be modelled by an effective friction on each particle. As the individual particles spin, their linear motion is subdued by a drag force as they slide, rather than roll, along the substrate. Meanwhile, this linear motion induces a velocity-dependent hydrodynamic interaction with the substrate that can in principle cause the particles to tilt away from the field rotation axis. As illustrated in Figure S2, this can lead to a rolling transverse to the motion of a particle. For a particle travelling with velocity u, the magnitude and orientation of these frictional forces can be represented by $\Gamma_u u$ and $\Gamma_\perp u_\perp$, respectively. The frictional coefficients Γ_u and $\Gamma_\perp$ make up the friction tensor Γ_{ij} that is permitted to sustain odd terms in a parity-breaking fluid.

To measure these frictional coefficients, we observe droplets of spinner fluid as they sediment along a substrate tilted at an angle φ as in Figure S5a. To extract the frictional coefficients from the resulting dynamics, we consider a simple model in the plane of the substrate, in which a particle experiences a longitudinal and transverse force due to Γ_u and $\Gamma_\perp$, and a gravitational force proportional to $g' = g \sin\varphi$ that balances the frictional forces. In this model, $\theta = \arctan(\Gamma_\perp/\Gamma_u)$ represents the angle of the motion of the particle with respect to g.

First, we measure the longitudinal substrate friction, Γ_u, by measuring the speed of the particles along the direction of gravity. The sedimentation speed v_{sed} (along $\theta = 0°$), the tilt angle of the substrate φ, and Γ_u are simply related by the force balance equation:

$$\Gamma_u v_{\text{sed}} = \rho g \sin\varphi \tag{S1}$$

where g is the gravity acceleration and the density ρ is computed by dividing the mass of a particle by the

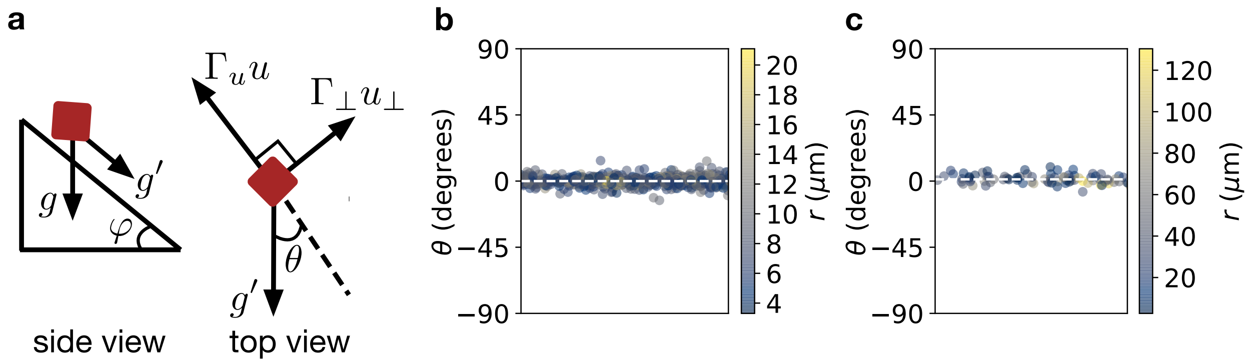

Supplementary Figure S5: **Characterization of transverse friction. a,** From the side, a particle sediments on an inclined substrate. However, from the top, we see that the sedimentation occurs at an angle θ due to a competition between gravity and friction. **b,** On a low-friction interface, the size of this sedimentation angle is small and independent of feature size, ranging from single particles to droplets of fluid. **c,** Similarly, the sedimentation angle is small on a high-friction interface.

average Voronoi cell area around a particle. We find, on a glass substrate,

$$\Gamma_{u,\mathrm{glass}} = 2.49 \pm 0.03 \times 10^3 \text{ Pa s/m}.$$

A similar experiment is performed for particles sedimented to soft interfaces. For curved droplets, we only measure v_{sed} over sufficiently small displacements such that particle trajectories are linear. This yields a substantially reduced substrate friction at air interfaces,

$$\Gamma_{u,\mathrm{air}} = 46 \pm 1 \text{ Pa s/m}.$$

At oil interfaces, we find Γ_u to increase with viscosity between $\Gamma_{u,\mathrm{air}}$ and $\Gamma_{u,\mathrm{glass}}$, as seen in Figure S9.

Then, to measure the transverse substrate friction, $\Gamma_\perp$, we measure θ for droplets ranging in size and moving at speeds on the order of u_{edge} (see Section 3.2). We observe $\theta = (0 \pm 3)^\circ$ on a low-friction interface and $\theta = (1 \pm 3)^\circ$ on a high-friction interface (see Figure S5b-c), allowing us to neglect $\Gamma_\perp$ in the remaining analysis: $\Gamma_\perp \ll \Gamma_u$. Meanwhile, the effect of a non-negligible transverse friction remains a fascinating problem that is addressed in Section 6.7.5.

3.2 Velocity profile and rotational and shear viscosities

We also measure the rotational and shear viscosities of the spinner fluid. We infer them from the vorticity profile in axisymmetric droplets. Practically, these quantities can be extracted by measuring how the velocity component tangent to the edge of a droplet varies in the direction normal to the edge of the droplet. We construct the velocity field of the spinner fluid from the instantaneous velocities of the particles, using a bin size of 2–4 microns.

We fit the radial velocity profile to a functional form obtained from the hydrodynamic equations, assuming rotational symmetry:

$$u(r) = 2\Omega\delta \frac{\eta_R I_1(r/\delta)}{\eta I_2(R/\delta) + \eta_R I_0(R/\delta)}, \tag{S2}$$

where

$$\delta = \sqrt{\frac{\eta + \eta_R}{\Gamma_u}}$$

is the penetration depth and I_k is a modified Bessel function of the first kind of order k (see Supplementary Section 6.2.1).

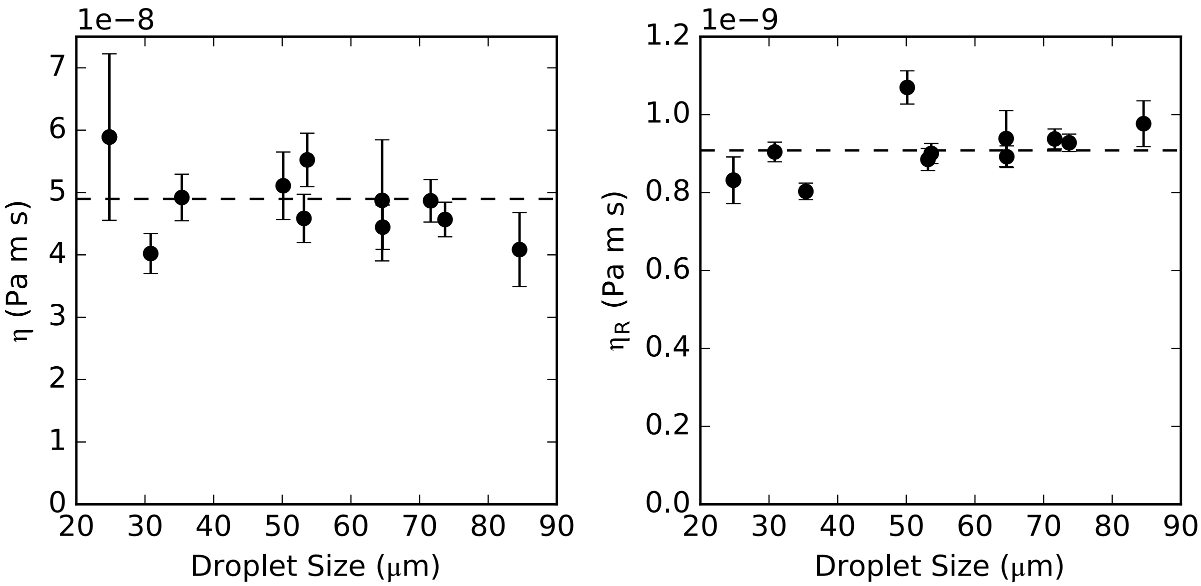

Supplementary Figure S6: **Measurement of viscosities.** By fitting the tangential velocity profiles to Eq. (S2), we measure the ordinary and rotational viscosities for a distribution of droplets larger than 4 penetration depths composed of particles spinning at 10 Hz. The dashed line shows the mean values.

A typical velocity profile, along with a best fit, is shown in Figure 3d in the main text. From this fit we extract the shear viscosity η, and rotational viscosity η_R (see Figure S6). We find, from an ensemble of measurements for droplets of varying size:

$$\eta_{\text{glass}} = 4.9 \pm 0.2 \times 10^{-8} \text{ Pa m s}$$

$$\eta_{R,\text{glass}} = 9.1 \pm 0.1 \times 10^{-10} \text{ Pa m s.}$$

Using these values above, we infer a penetration depth of

$$\delta_{\text{glass}} = 4.5 \pm 0.1\,\mu\text{m},$$

which corresponds to $\sim$2 particle layers. Figure S7 shows $u_{edge}/2\Omega\delta$ measured for different droplet sizes. For a droplet of radius $R = 50$ μm with particles spinning at 10 revolutions per second, we obtain an edge velocity $u_{\text{edge}} = u(R) = 11.7 \pm 0.2\,\mu$m/s.

At low-friction interfaces, the delocalized edge flow in the chiral fluid induces a background rotation by dragging the interface with it. We therefore add a rigid body rotation term of the form $\Omega_R r$ to our theoretical prediction for the tangential velocity profile. A sample fit, analogous to the profile provided for a droplet on a glass substrate (Figure 3d), demonstrates agreement to this form (see Figure S8a). We observe agreement between this procedure and a rigorous treatment of the flow profile incorporating the interaction of the chiral fluid with an interface, which we postpone to future work. Fitting to the form $u(r) + \Omega_R r$, we find a background rotation rate of $\Omega_R \sim 0.66$ 1/s and parameter estimates for a single droplet:

$$\eta_{\text{air}} = 2.5 \pm 0.4 \times 10^{-8} \text{ Pa m s}$$

$$\eta_{R,\text{air}} = 9.5 \pm 0.1 \times 10^{-10} \text{ Pa m s.}$$

These viscosity estimates are close to those on glass, but Γ_u is significantly decreased. Accordingly, we find a penetration depth of

$$\delta_{\text{air}} = 23.8 \pm 0.2\,\mu\text{m},$$

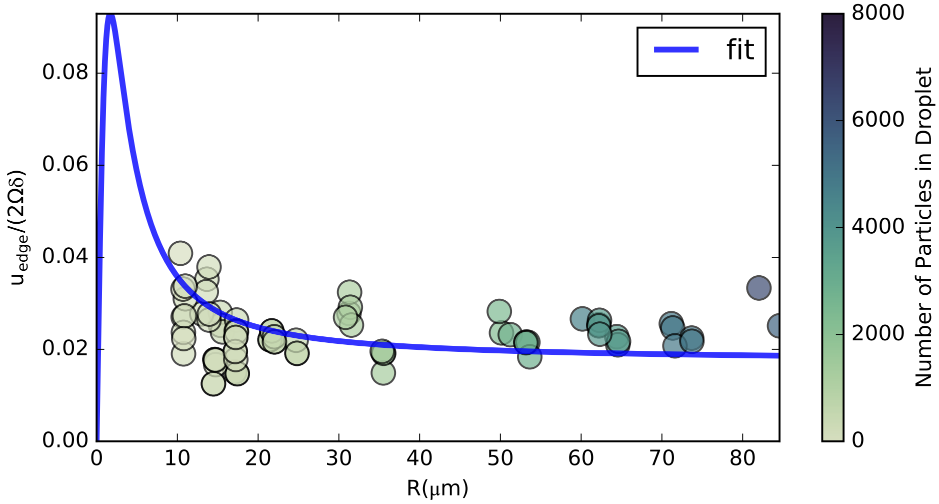

Supplementary Figure S7: **Extracting viscosities from velocity profiles.** We collect velocity profiles from droplets of spinner fluid and we extract the edge current velocity u_{edge} and penetration depth δ. The figure shows $u_{edge}/2\Omega\delta$ plotted against the droplet radius, R, for each droplet.

which demonstrates the delocalization of the edge current illustrated in Figure 4b.

We perform this fitting procedure for velocity profiles at oil interfaces of variable viscosity, again finding good agreement to the theory with an additional rigid body component. As the viscosity is increased, we expect a damping of the background fluid rotation. This expectation is supported by the decrease in the fit for Ω_R with increasing viscosity, as shown in Figure S8b. With this fitting approach, we find edge current localization to increase with the viscosity of the oil phase, as shown in Figure S9.

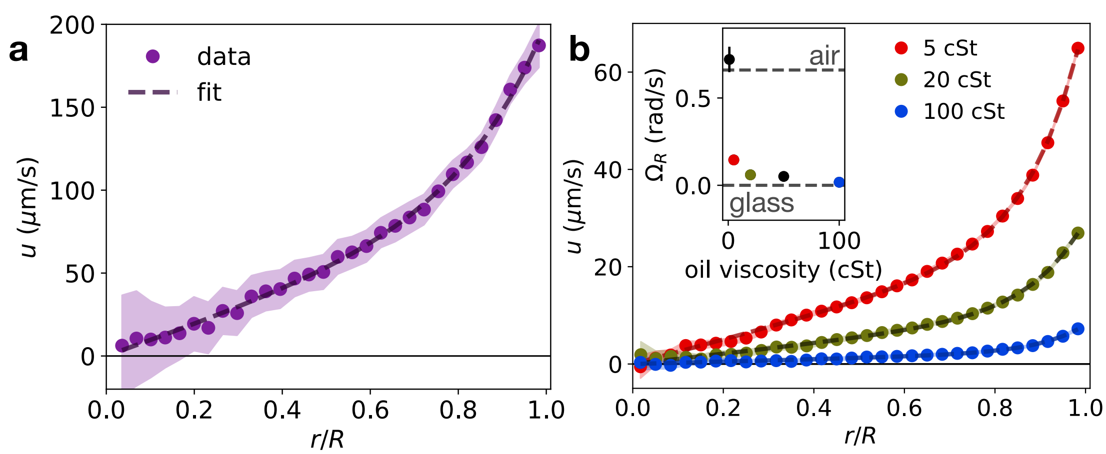

Supplementary Figure S8: **Velocity profiles with background rotation. a,** On a low-friction substrate, like the air-water interface, the edge current is delocalized (c.f. Figure 4b). To extract hydrodynamic parameters from the associated tangential velocity profile, $u(r)$, we fit to the radial theory (Eq. (S2)) with an additional rigid body rotation rate, yielding a good fit. **b,** A similar procedure accurately fits velocity profiles at oil interfaces, with both the velocity and the rigid body contribution decreasing with increasing viscosity.

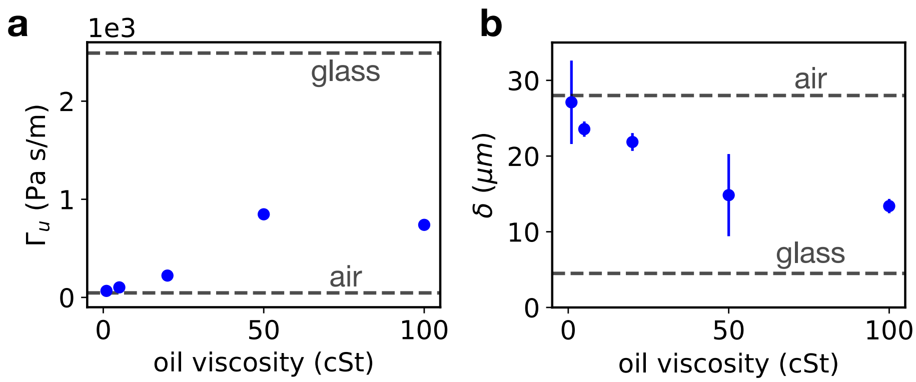

Supplementary Figure S9: **Tuning the substrate friction.** **a**, The spinner fluid sits at an interface with oil of viscosity that we can control. By increasing the viscosity, we increase the substrate friction, and **b**, decrease the penetration depth, partially spanning the region between the air and glass extremes.

4 Measurement of surface wave spectrum and dissipation

To measure the dispersion relation, we excite surface waves on straight strips or nearly-circular droplets of chiral fluid, prepared as in Section 2, either by briefly rolling particles in the direction perpendicular to the fluid, or by letting nearby droplets merge with it. We then spin the particles for about 10 minutes and let the perturbations evolve in time (see Supplementary Movie 7). As the strip or circular droplet equilibrates, small nearby clusters may coalesce with it, resulting in additional excitations.

We identify the edges of the strip or circular droplet by thresholding the images and using Canny edge detection. For the strip geometry, we take the height profile to be the distance from a straight line which spans the strip to the strip's perturbed edge. For the circular geometry, we take the radial profile to be the distance from the circumference of the droplet to its center of mass. For high-friction experiments, we record this height or radial profile over time at a sample rate between 1 fps and 4 fps. For low-friction experiments, the dynamics are substantially faster, so we record the same profile at a rate between 25 fps and 50 fps. We then perform a fast Fourier transform (FFT) on this data. We square the absolute value of this FFT to obtain a power spectrum in frequency ω, and wavenumber k. To obtain the final power spectrum we normalize each slice in k by the average power in that slice.

The resulting power spectrum shows dissipative waves with a clear dispersion relation in both geometries, as shown in the left panel of Figure S10 and in Figures 2b,c and Figures 4a,b. Taking the form of excitations to be proportional to $e^{i\omega t - \alpha t}$, where ω characterizes the propagation of waves and α the dissipation, the power $P_k(\omega)$ at each k is given by the relation

$$P_k(\omega) \propto \frac{1}{\alpha(k)^2 + [\omega - \omega(k)]^2}, \tag{S3}$$

where the functions $\omega(k)$ and $\alpha(k)$ define the dispersion relation and dissipation rate, respectively, of the linear waves.

There are often small background drifts in the chiral fluid which may result in a secondary linear feature in the power spectrum. While this additional feature varies between samples, the main dispersion curve remains unchanged. We thus fit the spectrum at each k to a sum of two peaks of the form in Eq. (S3) (see also right panel in Figure S10a). By selecting the peaks closest to the dispersion curve, we obtain the value of α at each k, as shown in Figure S10b).

For low-friction experiments, we observe a background rotation of the chiral fluid (see Section 3.2). As a result, we correct $\omega(k)$ by subtracting the background rate of the interface, Ω_R, in Figure 4b. This correction does not have any effect on the dissipation of waves $\alpha(k)$ as it preserves the width of the spectra at each k.

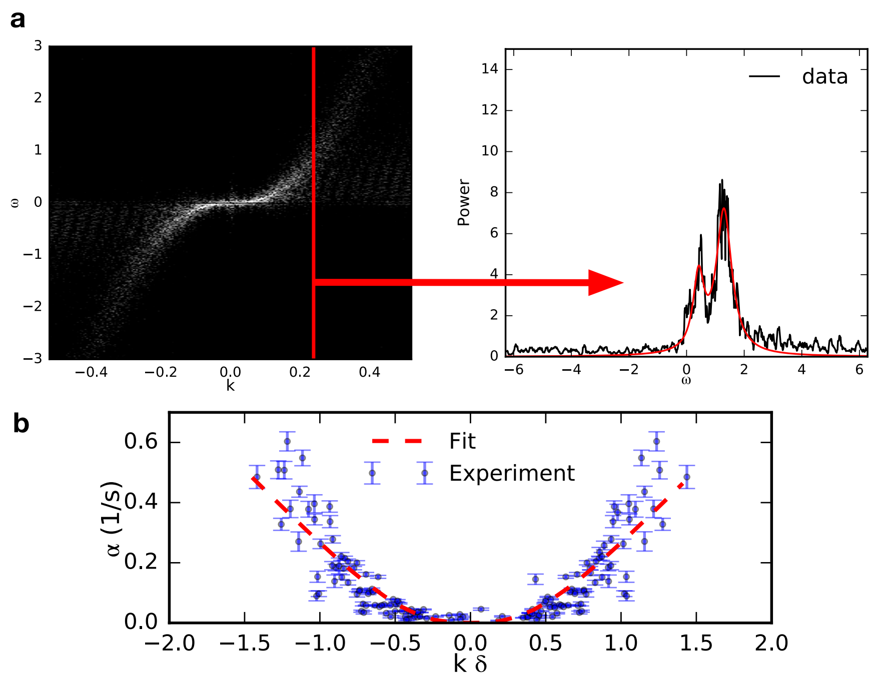

Supplementary Figure S10: **Extracting wave dissipation rates from the power spectrum. a,** By fitting each slice using the relation in Eq. (S3) we obtain values for the dissipation α at each wavenumber k. **b,** We fit these values to the analytical solution, to infer the fluid's surface tension. Shown with the red dashed line is a fit to the theoretical prediction for the damping rate of the chiral waves.

4.1 Fitting the dissipation

By fitting $\alpha(k)$ to the full analytical solution for the dissipation ignoring contributions from η_o (see Supplementary Section 6.4.4 for an asymptotic approximation in the strip geometry) we infer the surface tension of the fluid γ. At the glass interface and in the strip geometry, we find

$$\gamma_{\text{glass}} = 2.3 \pm 0.2 \times 10^{-13} \text{ N}.$$

We obtain the same result for a circular droplet geometry within measurement error. The fitted dissipation data are presented in Figure 4c (droplet) and Figure S10 (strip). When fitting to the full analytical solution for the dissipation adding contributions from η_o we obtain the same result for γ, with $\eta_{\text{o,glass}} = 0 \pm 2 \times 10^{-9}$ Pa m s.

On air interfaces, as shown in the main text, we are no longer able to fit the dissipation without including contributions from η_o. In this case, for a droplet geometry, we obtain

$$\gamma_{\text{air}} = 3.7 \pm 0.2 \times 10^{-13} \text{ N},$$

$$\eta_{o,\text{air}} = 1.5 \pm 0.1 \times 10^{-8} \text{ Pa m s}.$$

4.2 Disambiguating Hall viscosity and surface tension

As noted in the main text, disentangling the relative role of Hall viscosity η_o and surface tension γ relies on observing wave dissipation $\alpha(k)$ over a large range of rescaled wavelengths $k\delta$. On a glass substrate, the typical range of $k\delta$ is too small to observe these features. The dispersion $\omega(k)$ is not useful in lifting this ambiguity, because it is unchanged by the inclusion of non-zero η_{o}, as shown in Figure S11a. Moreover, the dissipation can be modeled by the hydrodynamic theory (see Supplementary Section 6.6) incorporating non-zero η_o by compensating with γ, as can be seen from the asymptotic form of $\alpha(k)$ at small $k\delta$, $\alpha \sim k^3(\gamma + \eta_{\text{o}})$ (see Section 6.4.4) and shown in Figure S11a.

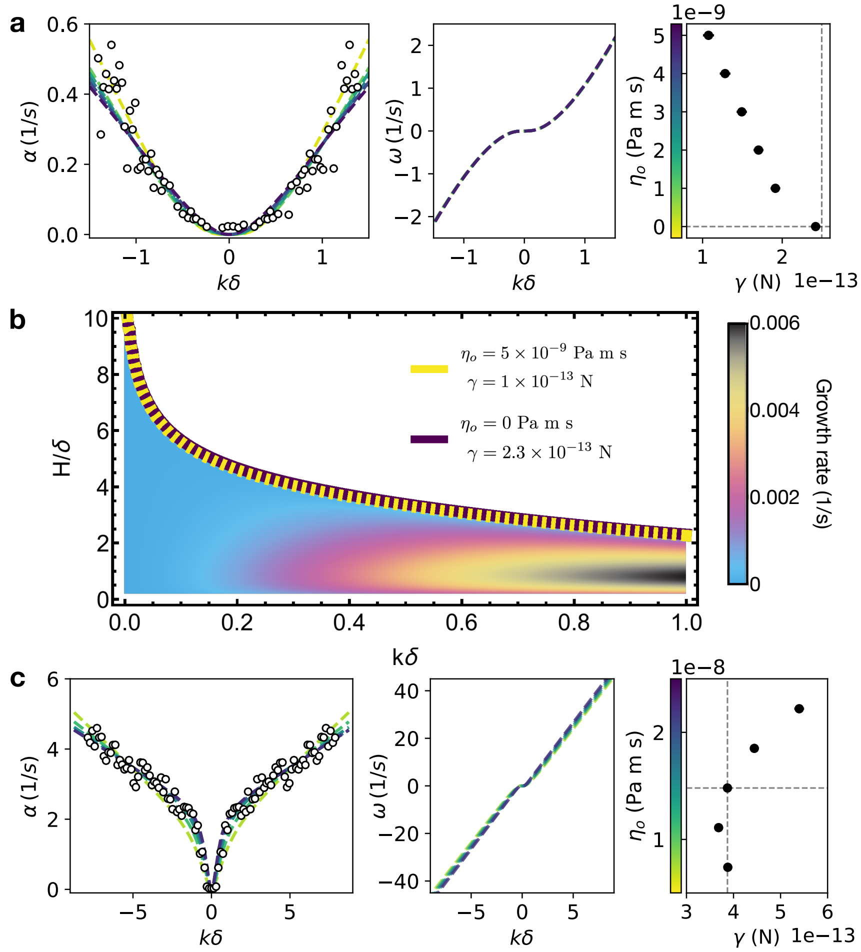

Supplementary Figure S11: **Disambiguating Hall viscosity and surface tension. a,** For high-friction experiments, the acquired wave dissipation data are limited to $k\delta \sim 1$, and can be fit to both zero and non-zero Hall viscosity (left), yielding no discrepancy in the dispersion (middle), by altering the apparent surface tension (right). **b,** The boundary between stable and unstable modes constructed using a non-zero value of Hall viscosity is indistinguishable from the boundary for $\eta_{\mathrm{o}} = 0$. Here, each boundary curve is shown over the calculated diagram for $\eta_{\mathrm{o}} = 0$. **c,** In the large $k\delta$ regime, similarly to **a**, we can fit the low-friction experimental data to a wide range of Hall viscosity values (left-middle), in this case finding an opposite correlation to **a** (right).

However, we obtain a clear signature of Hall viscosity in the dissipation when we decrease the substrate friction Γ_u, by replacing the glass substrate with an oil or air interface, as we demonstrate in the main text. By changing the oil viscosity we can tune Γ_u between these two regimes (see Section 2.3) and explore the emergence of this qualitative signature of Hall viscosity. This procedure regulates δ, thus controlling the range of $k\delta$ over which surface waves are observed. We plot the wave dissipation $\alpha(k)$ for representative values of oil viscosity in Figure S12. As the viscosity is decreased (and hence also the substrate friction), the presence of η_{o} is more discernible through leveling-off at large $k\delta$, and the quality of fits with $\eta_{\mathrm{o}} = 0$ becomes increasingly poor. By contrast, the dissipation on a high viscosity interface can be captured using both a non-zero or zero value of η_{o}, just as observed for the glass substrate experiments (c.f. Figure 4c).

We note that there is also an ambiguity in distinguishing the effects of Hall viscosity and surface tension for data containing wave dissipation at $k\delta \gg 1$. To see this, we fit $\alpha(k)$ for waves measured at an air interface to the full hydrodynamic theory for γ, by imposing values of η_{o} $\pm 50\%$ of $\eta_{\mathrm{o,air}}$. We find that the data is fit well for a wide range of values of η_{o} by tuning γ to compensate, as in Figure S11c. To explain the

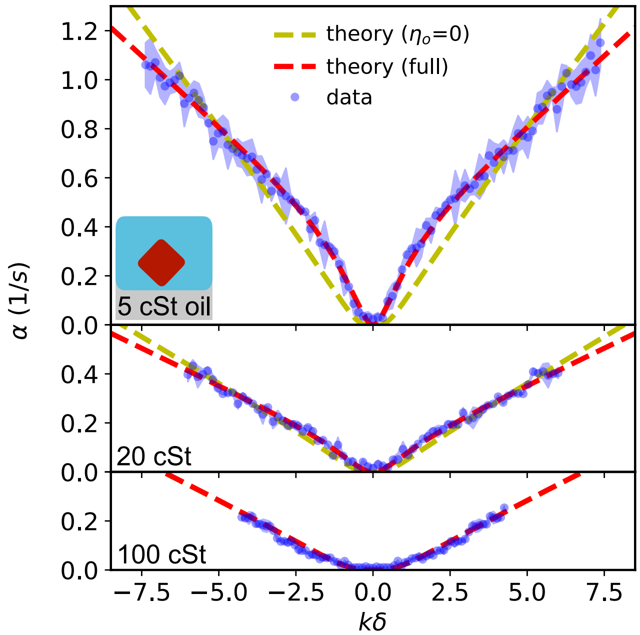

Supplementary Figure S12: **Hall viscosity emerges for low substrate friction.** When the spinner fluid is over a water-oil interface, the wave dissipation can be measured at larger $k\delta$ for lower viscosities of oil, which lead to lower substrate friction and thus larger penetration depth δ. With this extended scope, we are better able to distinguish the effects of surface tension γ and Hall viscosity η_o, by fitting to the theory with and without η_o.

correlation of η_o and γ in this regime, as presented in the right panel, we consider the large $k\delta$ asymptotic $\alpha \sim k\gamma/(1+\eta_\mathrm{o}^2)$. The dispersion does not resolve this correlation, as $\omega(k)$ is not strongly-dependent on η_o.

5 Characterization of the strip instability

We prepare strips of spinner fluid as described in Section 2. To get strips of different thicknesses, like the ones shown in Figure 4a of the main text and Supplementary Movie 11, we vary the concentration of the original suspension. We characterize the thickness of a strip before it goes unstable (if it does) by measuring the thickness at various points and taking the mean. To measure the wavelength of the instability in unstable strips, we take the fast Fourier transform of the strip's outline, as described in Section 4, up to the breakup point. The unstable modes appear as fast-growing peaks in this Fourier transform.

As explained in the main text, our intuitive understanding of the mechanism for the instability demands that the outline of the strips at the break-up point be asymmetric. We characterize this asymmetry by collecting the outlines at several of these break-up points, rescaling them by the strip thickness at the thinnest point and by the unstable wavelength in each case, and overlaying them, as shown in Figure 5c of the main text.

Just as the Hall viscosity fails to impact the propagation or dissipation of waves of our chiral fluid on a glass substrate, so too does it fail to alter the stability diagram. As in Figure S11b, we see that the line separating stable from unstable modes is nearly unchanged by the addition of an η_o associated with the maximal value in Figure S11a.

6 Hydrodynamic theory of the colloidal chiral fluid

6.1 Equations of motion

Building on previous work [5, 6, 7, 8, 9, 10, 11, 12], we describe our system with a continuum hydrodynamic theory. The hydrodynamic variables are the mass density of spinners $\rho(\mathbf{x}, t)$, the momentum density $\rho(\mathbf{x}, t)u_i(\mathbf{x}, t)$ and the angular momentum density $I_0\Omega(\mathbf{x}, t)$, where I_0 is the spinner moment of inertia density. The conservation of momentum, angular momentum, and mass yields two-dimensional hydrodynamic equations. The first is conservation of mass:

$$(\partial_t + \mathbf{u} \cdot \nabla + \nabla \cdot \mathbf{u})\, \rho = 0$$

We will assume incompressibility in the following, reducing the above to

$$\nabla \cdot \mathbf{u} = 0 \tag{S4}$$

The second is conservation of momentum. For a 2D homogeneous and isotropic fluid in contact with a solid substrate, it takes the generic form:

$$\rho\, (\partial_t + \mathbf{u} \cdot \nabla)\, u_i = -\partial_i p + \eta \nabla^2 u_i + \eta_D \partial_i (\nabla \cdot \mathbf{u}) + \eta_R \epsilon_{ij} \partial_j\, (2\Omega - \omega) - \Gamma_{ij} u_j + \eta_o \nabla^2 \epsilon_{ij} u_j, \tag{S5}$$

where ϵ_{ij} is the Levi-Civita symbol, p is the pressure, $\omega = \hat{\mathbf{z}} \cdot (\nabla \times \mathbf{u}) = \epsilon_{ij} \partial_i u_j$ is the vorticity (which in two dimensions is a scalar), η is the shear viscosity, η_D is the dilatational viscosity, η_R is the rotational viscosity, η_o is a pseudo-scalar material parameter known as the Hall viscosity (or odd viscosity) [9], and $\Gamma_{ij} u_j = (\Gamma_u \delta_{ij} + \Gamma_\perp \epsilon_{ij})\, u_j$ the frictional force with the substrate, which in principle allows for two independent longitudinal and transverse friction coefficients.

The dimensions of each quantity are: $[u] = L/T$, $[p] = M/T^2$, $[\rho] = M/L^2$, $[\omega] = 1/T = [\Omega]$, $[\Gamma_u] = [\Gamma_\perp] = M/(L^2 T)$, $[\eta] = [\eta_D] = [\eta_R] = [\eta_o] = M/T$.

The third is conservation of angular momentum:

$$I_0\, (\partial_t + \mathbf{u} \cdot \nabla + \nabla \cdot \mathbf{u})\, \Omega = -\Gamma^\Omega \Omega - 2\eta_R\, (2\Omega - \omega) + D_\Omega \nabla^2 \Omega + \tau, \tag{S6}$$

where Γ^Ω is the rotational friction, D_Ω is the angular momentum diffusion constant, and τ the torque density field experienced by the spinners. In principle, friction with the medium surrounding the fluid could give rise to a torque that is proportional to ω. For simplicity, we do not treat this contribution independently of Γ^Ω and η_R. The dimensions of each quantity are: $[I_0] = M$, $[D_\Omega] = ML^2/T$, $[\Gamma^\Omega] = M/T$, $[\tau] = M/T^2$.

To estimate the relative contributions of each term, we interpret its role and estimate its magnitude by dimensional analysis. η and η_R both originate in the stresses nearby particles exert on each other, principally through the lubrication layer that separates them. Their value will therefore be comparable to η_{H_20}, up to a geometric factor and the ratio of the densities of the spinner fluid and water. Our measurements confirm this. η_o also originates from the stresses nearby particles exert on each other but also depends on the extent of time-reversal symmetry breaking and is less straightforward to estimate. In theoretical studies of vortex fluids [11], electrons in magnetic fields [13, 14, 15], and fluids of chiral grains [12], $\rho\eta_o$ is proportional to the angular momentum per particle but we are not aware of a similar estimate in over-damped systems. We find from our measurement that η_o at typical frequencies of $\sim 10\,\mathrm{Hz}$ is comparable in magnitude to η. $(\Gamma_u/\rho)^{-1}$ corresponds to the time required to damp the linear motion of an individual colloid. From the sedimentation measurements this is $< 10^{-6}\,\mathrm{s}$. The sedimentation experiments also put an upper bound to the ratio $\Gamma_\perp/\Gamma_u$ which is found to be negligible with a properly balanced field orientation (see Sections 2.1 and 3.1). In all that follows, we therefore approximate the friction tensor by its longitudinal component: $\Gamma_{ij} \equiv \Gamma_u \delta_{ij}$. γ is estimated by U_{int}/a, where U_{int} is the time-averaged interaction potential between the hematite magnetic dipoles, $U_{\mathrm{int}} \sim \mu_0 \mu^2/a^3$, a is the typical particle spacing, and μ is the dipole moment [16]. This approximation yields $\gamma \sim 10^{-13}$ N, which is consistent with measurements.

If we take as a characteristic velocity $\Omega\delta$ and characteristic gradient $1/\delta$, we find that the ratio of the material derivative term on the LHS to terms on the RHS is $< 10^{-2}$. We thus neglect the material derivative terms on the LHS of the momentum and angular momentum equations. Further assuming constant density

$\rho \equiv \rho_0$ and spinning frequency $\Omega \equiv \Omega_0$ simplifies the problem considerably. The momentum equation Eq. (S5), using $\nabla \cdot \mathbf{u} = 0$, becomes:

$$\eta \nabla^2 u_i - \partial_i \tilde{p} + \eta_R \epsilon_{ij} \partial_j (2\Omega - \omega) - \Gamma_u u_i = 0 \tag{S7}$$

where $\tilde{p} = p + \eta_o \omega$ absorbs the bulk effects of Hall viscosity in an incompressible fluid. The bulk momentum equation is thus simply a Brinkman equation, as arises in modeling porous medium flow, with forcing by an anti-symmetric stress. The angular momentum equation Eq. (S6), using $\nabla \cdot \mathbf{u} = 0$, reduces to:

$$\frac{1}{2} \Gamma^\Omega \Omega + \eta_R (2\Omega - \omega) = \frac{\tau}{2} \tag{S8}$$

In this system of equations the pressure instantly adjusts to maintain the divergence-free condition, while the torque τ adjusts to enforce constant rate of rotation. Hence, only the momentum equation, with the divergence-free condition, is required to compute the bulk flow. Given a constant 2Ω, and using that $-\epsilon_{ij} \partial_j \omega = \nabla^2 u_i$, yields

$$\delta^2 \nabla^2 \mathbf{u} - \nabla \bar{p} - \mathbf{u} = \mathbf{0} \tag{S9}$$

or an (apparently) unforced Brinkman equation, where $\delta = ((\eta + \eta_R)/\Gamma_u)^{1/2}$ is the so-called hydrodynamic length, and $\bar{p} = \tilde{p}/(\Gamma_u)$. Note that the pressure satisfies $\nabla^2 \tilde{p} = 0$. Taking the curl and using the divergence-free condition yields

$$\delta^2 \nabla^2 \omega - \omega = 0 \tag{S10}$$

which is a screened Laplace (or Yukawa) equation for the vorticity. Both the Brinkman and Yukawa equations are solved as boundary value problems.

To consider free-surface flows, let D denote the chiral fluid domain in the plane, having boundary ∂D with outward facing normal $\hat{\mathbf{n}}$. If $\mathbf{v}$ is the velocity of ∂D, then we adopt the kinematic boundary condition

$$\mathbf{v} = \mathbf{u}|_{\partial D}, \tag{S11}$$

giving that the boundary moves with the fluid velocity. We also assume the stress balance equation:

$$\boldsymbol{\sigma} \hat{\mathbf{n}}|_{\partial D} = \gamma \kappa \hat{\mathbf{n}} \tag{S12}$$

where γ is the surface tension and κ is the curvature of ∂D. The stress tensor $\boldsymbol{\sigma}$ is given by:

$$\sigma_{ij} = -p\delta_{ij} + (\eta_D - \eta)\, \delta_{ij} \partial_k u_k + \eta_R \epsilon_{ij} (2\Omega - \omega) + 2\eta \frac{1}{2} (\partial_i u_j + \partial_j u_i) + \eta_o (\partial_i \epsilon_{jk} u_k + \epsilon_{ik} \partial_k u_j) \tag{S13}$$

$$= -(p - \eta_o \omega)\, \delta_{ij} + \eta_R \epsilon_{ij} (2\Omega - \omega) + 2\eta \frac{1}{2} (\partial_i u_j + \partial_j u_i) - \eta_o O_{ij}, \tag{S14}$$

where we have assumed $\partial_k u_k = 0$ and:

$$O_{ij} = \begin{pmatrix} -2\partial_y u_x & +2\partial_x u_x \\ -2\partial_y u_y & +2\partial_x u_y \end{pmatrix}. \tag{S15}$$

Eqs. (S4, S9, S11, S12) are a closed set determining the dynamics of the chiral fluid domain. It is solved as a free-boundary problem, with boundary conditions Eq. (S12) determining the instantaneous velocity field through solution of Eqs. (S4, S9). The boundary is then evolved via the kinematic boundary condition Eq. (S11).

Comments

A few comments are in order:

- While the local stress in our colloidal chiral fluid differs from the local stress in a Newtonian fluid, the resulting flow Eq. (S9) reduces to that of a Newtonian Brinkman fluid, implying that the bulk dynamics of Newtonian fluids and odd stress fluids are indistinguishable. The difference in the flows, and in particular the presence of surface edge-flows, arises from the difference in the stress at the boundary.

- The presence of an odd stress necessitates the application of a body torque by the following argument. Consider an infinitesimal region of characteristic size ℓ; the torque τ_k on this region is proportional to $\epsilon_{kij}\sigma_{ij}\ell^3$. The moment of inertia about the axis $\hat{x}_k$ is proportional to $\rho\ell^5$. Thus angular momentum conservation implies infinite acceleration as $\ell \to 0$. This implies that in the absence of a body torque there can be no antisymmetric component to the stress.

- The presence of an odd stress in Eq. (S9) breaks the invariance under parity transformations of the equations of motion. This can be seen by the following argument. Consider Eq. (S9), keeping in mind that it models a 2D fluid embedded in three-dimensional space:

$$\eta\nabla^2 u_i - \partial_i p + \eta_R \hat{z}_k \epsilon_{kij}\partial_j \left(2\Omega - \hat{z}\cdot\nabla\times u_i\right) - \Gamma_u u_i = 0$$

where u_i has no component in the $\hat{z}$ direction and is a function of (x, y) alone. Under the parity transformation $(x, y, z) \to (x, y, -z)$ the equation becomes:

$$\eta\nabla^2 u_i - \partial_i p + \eta_R \hat{z}_k \epsilon_{kij}\partial_j \left(-2\Omega - \hat{z}\cdot\nabla\times u_i\right) - \Gamma_u u_i = 0$$

demonstrating that if one does not also reverse the direction of spin of the colloids, the equation is in general not invariant. Of course in the case of constant spinning motion in which the parity breaking term vanishes, the flow equation is parity invariant. Parity remains, however, broken by the corresponding stress boundary condition.

- The presence of a Hall viscosity η_o in Eq. (S9) stems from the breaking of time-reversal symmetry in two dimensions [9, 10]. In theoretical studies of vortex fluids [11], electrons in magnetic fields [13, 14, 15] and fluids of chiral grains [12], $\rho\eta_o$ was shown to be proportional to the angular momentum per particle (or vortex circulation), but we are not aware of an estimate in active over-damped systems.

- In an incompressible fluid, Hall viscosity has no effect in the bulk, only on the boundary. As shown in Eqs. (S13) and (S14), the Hall stress tensor can be divided into a quantity with divergence that can be absorbed in the pressure and a component $-\eta_o O_{ij}$ which is divergence free: $\partial_j O_{ij} = 0$. The former has no effect in an incompressible fluid, however the latter gives rise to stresses on the boundary. In particular, using $O_{ij}n_j = -2\partial_s u_j$:

$$\sigma_o \mathbf{n} = -2\eta_o \partial_s \mathbf{u} = -2\left(\partial_s u_s - \frac{u_n}{R}\right)\hat{\mathbf{s}} - 2\left(\partial_s u_n + \frac{u_s}{R}\right)\hat{\mathbf{n}}$$

where R denotes the surface radius of curvature with the convention that a circular droplet has a positive radius of curvature. From this it can be seen that Hall viscosity acts purely on the boundary, generating boundary stresses in proportion to variations of the surface flow *along* the boundary.

6.2 The role of magnetism

Our colloidal system consists of magnetic particles suspended in water, and is thus reminiscent of conventional ferrofluids composed of magnetic nanoparticles suspended in water. In this section, we outline several key differences in the microscopic interactions that arise from the larger size of the magnetic particles. These differences conspire to reduce the importance of magnetic stresses in the hydrodynamic description, ultimately enabling us to accurately model our surface dynamics without explicit reference to magnetic stresses.

Crucially, Brownian dynamics do not play a significant role in our particle dynamics as evidenced by the following observations:

- Our magnetic particles sediment out of suspension. Their gravitational height is of the order of 20 nm. Thus, thermal fluctuations are not sufficient to keep the particles in suspension in the bulk.

- We observe that in the absence of magnetic field, the particles assemble into persistent magnetic chains that we have never observed to unbind.

- Within the range of magnetic fields used in our experiments the magnetic energy μB, where μ is the permanent dipole of the particles [16], is of the order of $\sim 10^3 k_{\mathrm{B}}T$ thereby making orientational thermal fluctuations marginal to the particles' orientational dynamics.

The reduced role of Brownian dynamics reduces the role of magnetic forces to providing cohesion to the fluid and to constraining the spinning rate of the particles to be constant. Therefore, unlike conventional ferrofluids, the cohesion of our 2D chiral fluid does not rely on molecular surface tension but instead on the interactions between the magnetic particles. Furthermore the magnitude of the fluid's magnetization is constant, and its orientation is tied to that of the particles that compose the fluid itself. Consequently, magnetism appears implicitly in our equations of motion through the torque density $\tau = \mu_0 \vec{M} \times \vec{H}$ that is balanced by rotational friction and odd stress. While this torque density is ultimately responsible for driving flows, just as in the case of ferrofluids [17, 18, 19], magnetic forces do not play a direct role in surface dynamics.

To highlight the essential effect of these differences on the interfacial dynamics, we explore below their impact on the celebrated Rosensweig surface instability [20].

6.2.1 Absence of Rosensweig surface instability

Physically, the difference between the classical un-saturated ferrofluid and our fluid has its origins in the fact that in the case of the induced field, the magnetization itself is augmented in the peaks of the perturbation, whereas in our case the magnetization is fixed. In a ferrofluid, the augmentation of the magnetization leads to a wavenumber-dependent magnetic stress that produces the famous spiking instability [20]. As noted above, unlike a conventional ferrofluid, our system sustains a uniform magnetization, which leads to important differences.

Let us first first reproduce the Rosensweig result for the stress in conventional ferrofluids, extended to rotating fields, then compute the magnetic stress in our fixed magnetization case and compare the two. In both calculations, we consider a semi-infinite geometry with magnetic fluid occupying the $(y < 0)$ half plane, with a sinusoidally perturbed interface $h = \epsilon \cos(kx)$.

6.2.1.1 Rosensweig instability in conventional ferrofluids. In the case of the conventional ferrofluid, we seek a solution for the magnetic potential ϕ from which the magnetic field $\mathbf{B} = \mu\mathbf{H}$, $\mathbf{H} = -\nabla\phi$ can be deduced. The magnetization $\mathbf{M} = (\mu/\mu_0 - 1)\mathbf{H}$ is taken to be $M(\cos\theta_R\hat{\mathbf{x}} + \sin\theta_R\hat{\mathbf{y}})$ deep in the ferrofluid phase. We then find

$$\begin{aligned}
\mathbf{H}^+ &= \frac{M}{\mu - \mu_0}\left(\mu_0\cos\theta_R\hat{\mathbf{x}} + \mu_0\sin\theta_R\hat{\mathbf{y}}\right) + \delta\mathbf{H}^+,\\
\mathbf{H}^- &= \frac{M}{\mu - \mu_0}\left(\mu_0\cos\theta_R\hat{\mathbf{x}} + \mu\sin\theta_R\hat{\mathbf{y}}\right) + \delta\mathbf{H}^-,
\end{aligned}$$

where $\delta\mathbf{H}^\pm = -\nabla\delta\phi^\pm$ represents the perturbation to the magnetic field due to the sinusoidal modification of the interface:

$$\begin{aligned}
\delta\phi^+ &= \epsilon\frac{Me^{ky}}{\mu + \mu_0}\mu_0\sin\left(kx - \theta_R\right),\\
\delta\phi^- &= \epsilon\frac{Me^{-ky}}{\mu + \mu_0}\left[\mu\sin(\theta_R)\cos(kx) + \mu_0\cos(\theta_R)\sin(kx)\right].
\end{aligned}$$

The $+$ expressions correspond to the solution in the lower half plane and the $-$ to the solution in the upper half plane. The field is perturbed as

$$\begin{aligned}
\delta\mathbf{H}^+ &= -\frac{\mu_0 Mke^{ky}}{\mu + \mu_0}k\epsilon\left[\cos\left(kx - \theta_R\right)\hat{\mathbf{x}} + \sin\left(kx + \theta_R\right)\hat{\mathbf{y}}\right],\\
\delta\mathbf{H}^- &= \frac{\mu_0 Mke^{-ky}}{\mu + \mu_0}\epsilon\cos\theta_R\left[-\cos\left(kx\right)\hat{\mathbf{x}} + \sin\left(kx\right)\hat{\mathbf{y}}\right] + \frac{\mu}{\mu + \mu_0}\sin\theta_R\left[\sin\left(kx\right)\hat{\mathbf{x}} + \cos\left(kx\right)\hat{\mathbf{y}}\right].
\end{aligned}$$

That the fields and potentials satisfy both Maxwell's equations and the boundary conditions, $\hat{\mathbf{n}} \times (\mathbf{H}^+ - \mathbf{H}^-) = 0$ and $\hat{\mathbf{n}} \cdot (\mathbf{H}^- - \mathbf{H}^+) = \hat{\mathbf{n}} \cdot \mathbf{M}$, can be verified by explicit computation.

From the above, we obtain $\mathbf{B}^+ = \mu \mathbf{H}^+$ and $\mathbf{B}^- = \mu_0 \mathbf{H}^-$. The spatially-varying magnetization is then given by

$$\mathbf{M} = M\left(\cos\theta_R \hat{\mathbf{x}} + \sin\theta_R \hat{\mathbf{y}}\right) - \frac{(\mu-\mu_0)Me^{ky}}{\mu+\mu_0} k\epsilon \left[\cos\left(kx-\theta_R\right) + \sin\left(kx-\theta_R\right)\right] \tag{S16}$$

Finally, to obtain the surface stress, we evaluate the stress tensor,

$$T^{\pm}_{ij} = -\tfrac{1}{2}\delta_{ij}\mathbf{B}^{\pm}\cdot\mathbf{H}^{\pm} + \tfrac{1}{2}\left(H^{\pm}_i B^{\pm}_j + H^{\pm}_j B^{\pm}_i\right),$$

inside and outside the magnetized region. The surface stress follows from $\sigma_{nn} = T^- \cdot \hat{\mathbf{n}} - T^+ \cdot \hat{\mathbf{n}}$. Evaluating yields a perturbation to the magnetic surface stress, $\delta\sigma_{nn} = \sigma_{nn} - \sigma_{nn}(\epsilon = 0)$, that is wavenumber-dependent and in-phase with the perturbation to the interface, pushing it to grow,

$$\delta\sigma_{nn} = -k\frac{\mu_0 M^2}{2}\epsilon\cos(kx)\left(\cos(2\theta_R) - \frac{\mu-\mu_0}{\mu+\mu_0}\right).$$

This expression agrees with the celebrated expression computed by Rosensweig for $\theta_R = \pi/2$ (magnetic field normal to the interface) [20]. Even when the stresses are averaged over a period of rotation, we find a destabilizing stress:

$$\langle\delta\sigma_{nn}\rangle_{\theta_R} = k\frac{M^2}{2}\epsilon\cos(kx)\frac{\mu-\mu_0}{\mu+\mu_0}. \tag{S17}$$

6.2.1.2 Magnetic stresses in a saturated colloidal fluid. Repeating the calculation for our fluid using a fixed magnetization $\mathbf{M} = M(\cos\theta_R \hat{\mathbf{x}} + \sin\theta_R \hat{\mathbf{y}})$ in contrast to the spatially-varying magnetization of Eq. (S16), we find:

$$\begin{aligned}
\delta\phi^+ &= \epsilon\frac{Me^{|k|y}}{2}\left[\frac{k}{|k|}\cos\theta_R \sin kx - \sin\theta_R \cos kx\right],\\
\delta\phi^- &= \epsilon\frac{Me^{-|k|y}}{2}\left[\frac{k}{|k|}\cos\theta_R \sin kx + \sin\theta_R \cos kx\right],
\end{aligned}$$

The magnetic field is given by

$$\begin{aligned}
\mathbf{H}^+ &= -\frac{M}{2}\sin\theta_R \hat{\mathbf{y}} + \delta\mathbf{H}^+,\\
\mathbf{H}^- &= \frac{M}{2}\sin\theta_R \hat{\mathbf{y}} + \delta\mathbf{H}^-,
\end{aligned}$$

where the perturbative pieces are

$$\begin{aligned}
\delta\mathbf{H}^+ &= -\epsilon\frac{Me^{|k|y}}{2}\left[\left(\frac{k^2}{|k|}\cos\theta_R\cos kx + k\sin\theta_R \sin kx\right)\hat{\mathbf{x}} + \left(k\cos\theta_R \sin kx - |k|\sin\theta_R\cos kx\right)\hat{\mathbf{y}}\right],\\
\delta\mathbf{H}^- &= \epsilon\frac{Me^{-|k|y}}{2}\left[\left(k\sin\theta_R\sin kx - \frac{k^2}{|k|}\cos\theta_R \cos kx\right)\hat{\mathbf{x}} + \left(k\cos\theta_R \sin kx + |k|\sin\theta_R\cos kx\right)\hat{\mathbf{y}}\right].
\end{aligned}$$

Then, using $\mathbf{B}^- = \mu_0\mathbf{H}^-$ and $\mathbf{B}^+ = \mu_0(\mathbf{H}^+ + \mathbf{M})$, we can obtain the magnetic stress as above. In this case, the perturbation to the magnetic interfacial stress is:

$$\delta\sigma_{nn} = -k\frac{\mu_0 M^2}{4}\epsilon\left[\sin\left(2\theta_R\right)\sin kx + \mathrm{sgn}(k)\cos\left(2\theta_R\right)\cos kx\right].$$

When averaged over a period of rotation, $\langle\delta\sigma_{nn}\rangle_{\theta_R} = 0$, and:

$$\langle\sigma_{nn}\rangle_{\theta_R} = \frac{\mu_0 M^2}{8}. \tag{S18}$$

we find that, by comparison to Eq. (S17), the wavenumber-dependent part of the magnetic stress vanishes, leaving a constant magnetic pressure that would fail to drive the lively dynamics observed in our experiments.

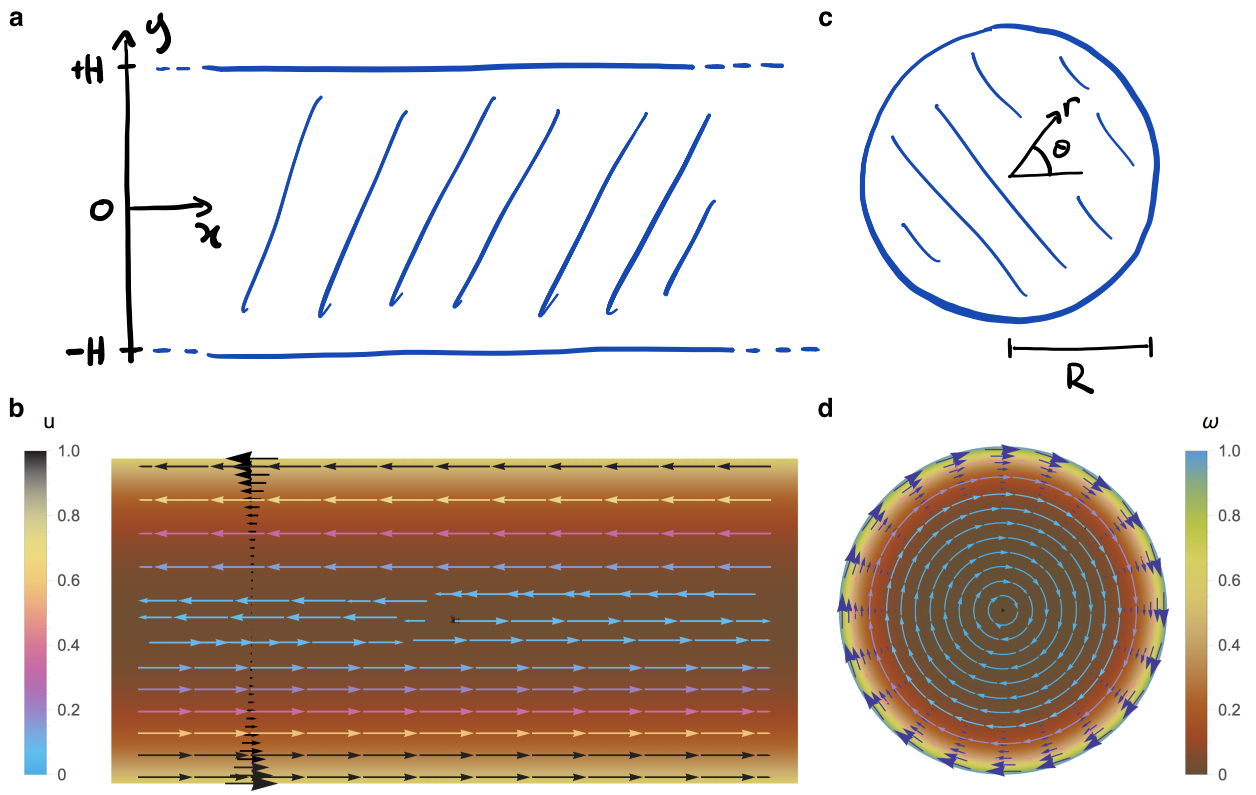

Supplementary Figure S13: **The geometry of steady edge currents in a circular droplet and in a slab of chiral fluid.** **a**, Setting variables describing a chiral fluid slab of thickness $2H$. **b**, Chiral fluid flow field within the slab. **c**, Setting variables describing a circular chiral fluid droplet of radius R. **d**, Chiral fluid flow field in the droplet. In **b** and **d** the background color represents the magnitude of vorticity and the arrows represent the direction of flow, colored by the velocity magnitude. Note that in both cases, the flow speed drops exponentially to zero as we move away from the boundary.

6.3 Steady-state solutions

We solve the hydrodynamic equations exactly for a circular droplet and in a slab geometry, as depicted in Figure S13.

6.3.1 The semi-infinite geometry

Consider a chiral fluid that occupies the region $y < 0$ of a plane. It is easy to verify that the following expression for ω satisfies the bulk equation (Eq. (S10)):

$$\omega = \frac{\eta_R}{\eta + \eta_R} 2\Omega e^{y/\delta}. \tag{S19}$$

for $|y| \leq 0$. The corresponding velocity has a non-zero component only in the $\hat{\mathbf{x}}$ direction and can be obtained by direct integration:

$$u_x = -\frac{\eta_R}{\eta + \eta_R} 2\Omega\delta e^{y/\delta}$$

The kinematic boundary condition is satisfied as there is no vertical component to the velocity. The normal stress boundary condition reduces to $\sigma_{yy} = p = p_0$ where p_0 is the pressure outside the slab which can be set to zero. The tangential stress boundary condition reduces to: $\sigma_{yx} = 2\eta_R\Omega - (\eta + \eta_R)\omega|_{y=0} = 0$, which is satisfied by Eq. (S19).

6.3.2 The slab geometry

Consider a slab of chiral fluid with thickness H, as depicted in Figure S13a. It is easy to verify that the following expression for ω satisfies the bulk equation (Eq. (S10)):

$$\omega = \frac{\eta_R}{\eta + \eta_R} 2\Omega \frac{\cosh\left(\frac{y}{\delta}\right)}{\cosh\left(\frac{H}{\delta}\right)}. \tag{S20}$$

for $|y| \leq H$. The corresponding velocity has a non-zero component only in the $\hat{\mathbf{x}}$ direction and can be obtained by direct integration:

$$u_x = -\frac{\eta_R}{\eta + \eta_R} 2\Omega\delta \frac{\sinh\left(\frac{y}{\delta}\right)}{\sinh\left(\frac{H}{\delta}\right)}$$

As in the case of the semi-infinite slab, the kinematic boundary condition is satisfied as there is no vertical component to the velocity. The normal stress boundary condition reduces to $\sigma_{yy} = p = p_0$ where p_0 is the pressure outside the slab which can be set to zero. The tangential stress boundary condition reduces to: $\sigma_{yx} = 2\eta_R\Omega - (\eta + \eta_R)\omega|_{y=\pm H} = 0$, which is satisfied by Eq. (S20).

Figure S13b depicts the flow field which consists of a left-moving, exponentially decaying current on the top surface and a right-moving, exponentially decaying current on the bottom surface.

6.3.3 The droplet geometry

Consider a circular droplet of chiral fluid with radius R, as depicted in Figure S13c. In cylindrical coordinates, assuming an azimuthal flow field $\mathbf{u} = u(r)\hat{\theta}$ and $\omega = \frac{1}{r}\partial_r(ru(r))$, we have for the radial component of the pressure: $\partial_r p(r) = 0$ and for the azimuthal component of the momentum equation:

$$r^2\partial_r^2 u + r\partial_r u - \left(1 + \frac{1}{\delta^2}r^2\right)u = 0$$

which is satisfied by $u(r) = AI_1(r/\delta)$ where I_1 is a modified Bessel function of the first kind. The boundary conditions $\sigma\hat{\mathbf{r}} = -\frac{\gamma}{R}\hat{\mathbf{r}}$ then fixes the constants p and A giving:

$$p = \frac{\gamma}{R} + \eta_o\frac{u(R)}{R} + p_0$$

and

$$u(r) = \frac{\eta_R I_1(r/\delta)}{\eta I_2\left(\frac{R}{\delta}\right) + \eta_R I_0\left(\frac{R}{\delta}\right)} 2\Omega\delta$$

for $0 \leq r \leq R$. The corresponding vorticity distribution is:

$$\omega(r) = \frac{\eta_R I_0(r/\delta)}{\eta I_2\left(\frac{R}{\delta}\right) + \eta_R I_0\left(\frac{R}{\delta}\right)} 2\Omega.$$

6.4 Perturbation of flow in a semi-infinite slab

In this section, we outline a calculation of the response of the otherwise flat interface of a chiral fluid that occupies the region $y \leq 0$.

6.4.1 Linearization scheme

Consider a flat interface at $y = 0$ which we perturb with a zero-mean perturbation $y = h(x,t) = \varepsilon g(x,t)$ with $\varepsilon << 1$. We represent the steady-state velocity, vorticity, and stress fields as $\bar{\mathbf{u}} = (\bar{u}, \bar{v})$, $\bar{\omega}$, and $\bar{\sigma}$, respectively, and introduce perturbations as

$$
\begin{aligned}
u(x,y) &= \bar{u}(y) + \varepsilon\tilde{u}(x,y) \\
v(x,y) &= \varepsilon\tilde{v}(x,y) \\
\omega &= \bar{\omega}(y) + \varepsilon\tilde{\omega}(x,y) \\
\boldsymbol{\sigma} &= \bar{\boldsymbol{\sigma}}(y) + \varepsilon\tilde{\boldsymbol{\sigma}}(x,y) \\
p &= \varepsilon q(x,y)
\end{aligned}
$$

6.4.2 Linear theory

Within this linearization scheme, the linearized equations and boundary conditions for the perturbed slab can be derived as follows.

6.4.2.1 Linearized bulk equations The linearized bulk equations are simply given by:

$$\left(\bar{\eta}\nabla^2 - \Gamma_u\right)\tilde{u}_i = \partial_i q \quad \text{and} \quad \nabla\cdot\tilde{\mathbf{u}} = 0 \tag{S21}$$

where $\bar{\eta} = \eta + \eta_R$.

6.4.2.2 Linearized stress boundary conditions The stress boundary conditions relate the bulk fields to interfacial data. We take an upward normal $\hat{\mathbf{n}} \approx \hat{\mathbf{y}} - \varepsilon g_x\hat{\mathbf{x}}$ and the RHS of Eq. (S12) is to linear order $\gamma\kappa\hat{\mathbf{n}} \approx \varepsilon\gamma g_{xx}\hat{\mathbf{y}}$. Expanding Eq. (S12) to linear order, and using that $\bar{\sigma}(0)\hat{\mathbf{y}} = \mathbf{0}$ yields

$$\tilde{\boldsymbol{\sigma}}(x,0)\hat{\mathbf{y}} = \gamma g_{xx}(x)\hat{\mathbf{y}} + g_x(x)\bar{\boldsymbol{\sigma}}(0)\hat{\mathbf{x}} - g(x)\bar{\boldsymbol{\sigma}}_y(0)\hat{\mathbf{y}}$$

After some simplification we obtain:

$$
\begin{aligned}
&\bar{\eta}\tilde{u}_y(x,0) + (\eta-\eta_R)\tilde{v}_x(x,0) + 2\eta_o\tilde{u}_x(x,0) = \bar{\eta}\bar{\omega}_y(0)\,g(x) + 2\eta_o\bar{\omega}(0)g_x(x) \\
&2\eta\tilde{v}_y(x,0) - q(x,0) + 2\eta_o\tilde{v}_x(x,0) = \gamma g_{xx}(x) - \left[(\eta-\eta_R)\bar{\omega}(0) + 2\eta_R\Omega\right]g_x(x)
\end{aligned}
\tag{S22}
$$

6.4.2.3 Linearized kinematic boundary condition The linearized kinematic boundary condition is given by:

$$g_t + \bar{u}(0)\,g_x = \tilde{v}(x,0) \tag{S23}$$

6.4.3 Solution

To solve Eqs. (S21, S22, S23) we make use of Fourier transforms in the x direction to take advantage of translational invariance.

6.4.3.1 Solution of the linearized bulk equations Taking the Fourier transform in x:

$$\bar{\eta}\left(\partial_{yy} - k^2\right)\tilde{\mathbf{u}} - \Gamma_u\tilde{\mathbf{u}} - (ik,\partial_y)\,q = \mathbf{0} \quad \text{and} \quad (ik,\partial_y)\cdot\tilde{\mathbf{u}} = 0$$

Using that $\left(\partial_{yy} - k^2\right)q = 0$ we obtain:

$$
\begin{aligned}
q &= Ae^{|k|y} \\
\tilde{u} &= -\frac{ik}{\bar{\eta}}\delta^2 Ae^{|k|y} + Be^{|\star|y} \\
\tilde{v} &= -\frac{|k|}{\bar{\eta}}\delta^2 Ae^{|k|y} - \frac{ik}{|\star|}Be^{|\star|y} \\
\tilde{u}_y &= -\frac{ik\,|k|}{\bar{\eta}}\delta^2 Ae^{|k|y} + |\star|\,Be^{|\star|y} \\
\tilde{v}_y &= -\frac{|k|^2}{\bar{\eta}}\delta^2 Ae^{|k|y} - ikBe^{|\star|y}
\end{aligned}
\tag{S24}
$$

Where $\star^2 = k^2 + \delta^{-2}$. The coefficients A and B are to be determined from the boundary conditions.

6.4.3.2 Application of the stress boundary conditions

Inserting Eq. (S24) into the linearized stress boundary conditions, Eq. (S22), yields:

$$\begin{aligned}\left[-2ik\,|k|\,\delta^2\frac{\eta}{\bar{\eta}}+2k^2\delta^2\frac{\eta_o}{\bar{\eta}}\right]A+\left[\frac{2\eta k^2+\bar{\eta}\delta^{-2}}{|\star|}+2ik\eta_o\right]B &= 2\left[\frac{\bar{\eta}}{\delta}+2ik\eta_o\right]\frac{\eta_R}{\bar{\eta}}\Omega g\\ \left[\left(1+2k^2\delta^2\frac{\eta}{\bar{\eta}}\right)+2ik|k|\delta^2\frac{\eta_o}{\eta}\right]A+\left[2ik\eta-2\eta_o\frac{k^2}{|\star|}\right]B &= \gamma k^2-4ik\eta_R\frac{\eta}{\bar{\eta}}\Omega g\end{aligned}$$

which is a set of two linear equations for the unknowns A, B in terms of the surface perturbation amplitude g.

6.4.3.3 Application of the kinematic boundary condition

Combining this with the kinematic boundary condition:

$$g_t + ik\bar{u}g = \tilde{v}$$

and substituting $\tilde{v}$ we can then compute the time evolution of a surface perturbation. In the section that follows, we discuss this evolution in the case of a sinusoidal perturbation of the height $g \sim \mathrm{Re}\left[e^{ikx}\right]$.

6.4.4 Visualization and asymptotics

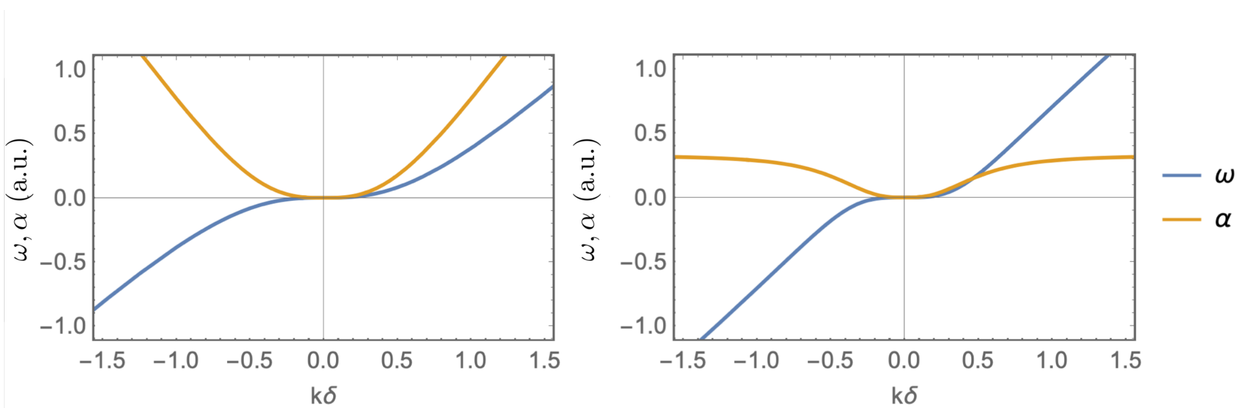

Supplementary Figure S14: **Typical dependence of surface wave dispersion and dissipation on wavenumber** (a) The dispersion and dissipation in the absence of Hall viscosity and for finite surface tension (b) The dispersion and dissipation in the absence of surface tension in the presence of Hall viscosity. The wavenumber dependence of dispersion is generically $\propto k^n$ for odd $n \geq 3$ for small k and $\propto k$ for large k. Similarly, the wavenumber dependence of dissipation is generically $\propto |k|^n$ for odd $n \geq 3$ for small k and $\propto |k|$ for large k.

The evolution of the surface corresponding to an infinitesimal sinusoidal perturbation of the height $g \sim \mathrm{Re}\left[e^{ikx}\right]$ is given by $g \sim \mathrm{Re}\left[e^{i(kx+\omega t)}e^{-\alpha t}\right]$ which corresponds to damped waves with dispersion $\omega(k\delta)$ and dissipation rate $\alpha(k\delta)$. Figure S14 shows typical wavenumber dependences $\omega(k\delta)$ and $\alpha(k\delta)$. From the anti-symmetry of the dispersion relation it can be seen that the surface waves are uni-directional. It is instructive to consider the long wavelength ($|k\delta| \ll 1$) and short wavelength ($|k\delta| \gg 1$) limits. The asymptotic expressions are given by:

$$\omega(k) = \begin{cases} 2u_{\mathrm{edge}}\dfrac{\eta}{\Gamma_u}k^3 & |k\delta| \ll 1 \\ -\dfrac{2\eta_R(\eta+2\eta_R)\Omega}{\eta^2+4\eta\eta_R+\eta_o^2+4\eta_R^2}+\left[\dfrac{1}{2}\dfrac{\gamma\eta_o}{\eta^2+\eta_o^2}\dfrac{(\eta^2+2\eta\eta_R+\eta_o^2+2\eta_R^2)}{(\eta^2+4\eta\eta_R+\eta_o^2+4\eta_R^2)}+u_{\mathrm{edge}}\right]k & |k\delta| \gg 1 \end{cases}$$

$$
\alpha(k) = \begin{cases} \left[\dfrac{\gamma}{\Gamma_u} + \dfrac{2\eta_o u_{\text{edge}}}{\Gamma_u}\right] |k|^3 & |k\delta| \ll 1 \\ \dfrac{2\eta_o \eta_R \Omega}{(\eta + 2\eta_R)^2 + \eta_o^2} + \left[\dfrac{\gamma(\eta+\eta_R)}{2\left(\eta^2+\eta_o^2\right)} \dfrac{\left(\eta^2 + 2\eta\eta_R + \eta_o^2\right)}{\left(\eta^2 + 4\eta\eta_R + \eta_o^2 + 4\eta_R^2\right)}\right] |k| & |k\delta| \gg 1 \end{cases}
$$

The dispersion relation at high wavenumbers (short wavelengths compared to δ) is generally linear, corresponding to waves with a constant speed, while at short wavenumbers (long wavelengths compared to δ) it scales with k^3. Similarly, the dissipation rate displays a transition at small wavenumbers from $|k|^3$ to a linear scaling at larger wavenumbers.

In order to gain insight on the physical origin of wave propagation and damping, it is instructive to consider the independent contributions of inter-rotor friction, odd viscosity and surface tension to dispersion and dissipation.

6.4.4.1 $\eta_o = \gamma = 0,\ \eta_R \neq 0$ In this limit surface waves are undamped, as $\alpha(k) = 0$, and the dispersion relation is given simply by:

$$
\omega(k) = \begin{cases} 2u_{\text{edge}} \dfrac{\eta}{\Gamma_u} k^3 & |k\delta| \ll 1 \\ -\dfrac{2\eta_R \Omega}{\eta + 2\eta_R} + u_{\text{edge}} k & |k\delta| \gg 1 \end{cases}
$$

The physical origin of these freely propagating waves can be understood, in the long wavelength limit, in terms of a curvature-dependent resistance to the flow of the surface boundary layer, as discussed in Section 6.7. In the short wavelength limit, the linear dispersion corresponds to simple advection of perturbations by the edge current.

6.4.4.2 $\eta_o = 0,\ \gamma \neq 0,\ \eta_R \neq 0$ In this limit the dispersion relation is unchanged, but the surface fluctuations are now damped by surface tension:

$$
\alpha(k) = \begin{cases} \dfrac{\gamma}{\Gamma_u} |k|^3 & |k\delta| \ll 1 \\ \dfrac{\gamma(\eta + \eta_R)}{2(\eta^2 + 2\eta\eta_R)} |k| & |k\delta| \gg 1 \end{cases}
$$

Thus surface tension has a purely dissipative effect on surface waves. This is a consequence of the lack of inertia in our system: surface tension acts to flatten the interface which, once flattened, remains so.

6.4.4.3 $\eta_o \neq 0,\ \gamma = 0,\ \eta_R \neq 0$ As in the case for $\eta_o = 0$, the dispersion relation at large wavenumbers converges to a linear one with slope u_{edge} and only the intercept is modified to: $-\frac{2\eta_R(\eta+2\eta_R)\Omega}{\eta^2+4\eta\eta_R+\eta_o^2+4\eta_R^2}$ to reflect the dominant wave-propagating mechanism at play (edge-pumping or capillary-Hall driving). The dissipation, however, is strongly affected:

$$
\alpha(k) = \begin{cases} \dfrac{2\eta_o u_{\text{edge}}}{\Gamma_u} |k|^3 & |k\delta| \ll 1 \\ \dfrac{2\eta_o \eta_R \Omega}{(\eta + 2\eta_R)^2 + \eta_o^2} & |k\delta| \gg 1 \end{cases}
$$

In both limits, the Hall stress η_o in conjunction with the odd stress η_R damps the surface waves. At long wavenumbers the scaling is akin to that given by surface tension, but at large wavenumbers the scaling is wavenumber-independent. We discuss the origin of this damping in Section 6.7.

6.4.4.4 $\eta_o \neq 0,\ \gamma \neq 0,\ \eta_R = 0$ In this case, there is no edge current and the dynamics come from a balance of surface tension, Hall viscosity and substrate friction:

$$
\omega(k) = \begin{cases} 4\dfrac{\gamma\eta_o}{\Gamma_u^2} k^5 & |k\delta| \ll 1 \\ \dfrac{1}{2} \dfrac{\gamma\eta_o}{\eta^2 + \eta_o^2} k & |k\delta| \gg 1 \end{cases}
$$

and:

$$\alpha(k) = \begin{cases} \dfrac{\gamma}{\Gamma_u}|k|^3 & |k\delta| \ll 1 \\ \dfrac{1}{2}\dfrac{\gamma\eta}{\eta^2+\eta_o^2}\;|k| & |k\delta| \gg 1 \end{cases}$$

which corresponds to damped unidirectional surface waves driven by a combination of surface tension and Hall viscosity. The driving mechanism for these waves can be understood in terms of a sequential mechanism in which surface tension drives a normal flow, and odd viscosity translates this into a propagation as discussed in Section 6.7.

6.4.4.5 The full dispersion is a combination of all these effects. Our unidirectional surface waves can be driven by differential drag on the boundary current or Hall viscosity acting in conjunction with surface tension. They are damped by surface tension and Hall viscosity acting in concert with the boundary current.

6.5 Perturbation of flow in a finite slab

We now examine the response of the steady-state slab solution to small perturbations from the bounding surfaces being flat.

6.5.1 Linearization scheme

Consider a flat interface at $y = 0$ which we perturb with a zero-mean perturbation $y = h\,(x,t) = \varepsilon g\,(x,t)$ with $\varepsilon << 1$. We will shift this result to the upper and lower surfaces when needed. We represent the steady-state velocity, vorticity, and stress fields as $\bar{\mathbf{u}} = (\bar{u}, \bar{v})$, $\bar{\omega}$, and $\bar{\sigma}$, respectively, and introduce perturbations as

$$\begin{aligned} u\,(x,y) &= \bar{u}\,(y) + \varepsilon\tilde{u}\,(x,y) \\ v\,(x,y) &= \varepsilon\tilde{v}\,(x,y) \\ \omega &= \bar{\omega}\,(y) + \varepsilon\tilde{\omega}(x,y) \\ \boldsymbol{\sigma} &= \bar{\boldsymbol{\sigma}}(y) + \varepsilon\tilde{\boldsymbol{\sigma}}(x,y) \\ p &= \varepsilon q(x,y) \end{aligned}$$

6.5.2 Linear theory

In this section we derive the linearized equations for the perturbed slab.

6.5.2.1 Linearized bulk equations The linearized bulk equations are given by:

$$\left(\bar{\eta}\nabla^2 - \Gamma_u\right)\tilde{u}_i = \partial_i q \quad \text{and} \quad \nabla\cdot\tilde{\mathbf{u}} = 0 \tag{S25}$$

where $\bar{\eta} = \eta + \eta_R$.

6.5.2.2 Linearized stress boundary conditions The stress boundary conditions relate the bulk fields to interfacial data. We take an upward normal $\hat{\mathbf{n}} \approx \hat{\mathbf{y}} - \varepsilon g_x\hat{\mathbf{x}}$ and the RHS of Eq. (S12) is to linear order $\gamma\kappa\hat{\mathbf{n}} \approx \varepsilon\gamma g_{xx}\hat{\mathbf{y}}$. Expanding Eq. (S12) to linear order, and using that $\bar{\sigma}(0)\hat{\mathbf{y}} = \mathbf{0}$ yields

$$\tilde{\boldsymbol{\sigma}}(x,0)\hat{\mathbf{y}} = \gamma g_{xx}(x)\hat{\mathbf{y}} + g_x(x)\bar{\boldsymbol{\sigma}}(0)\hat{\mathbf{x}} - g(x)\bar{\boldsymbol{\sigma}}_y(0)\hat{\mathbf{y}}$$

After some simplification we obtain:

$$\begin{aligned} \bar{\eta}\tilde{u}_y\,(x,0) + (\eta-\eta_R)\,\tilde{v}_x\,(x,0) + 2\eta_o\tilde{u}_x\,(x,0) &= \bar{\eta}\bar{\omega}_y\,(0)\,g(x) + 2\eta_o\bar{\omega}(0)g_x(x) \\ 2\eta\tilde{v}_y\,(x,0) - q\,(x,0) + 2\eta_o\tilde{v}_x\,(x,0) &= \gamma g_{xx}(x) - \left[(\eta-\eta_R)\,\bar{\omega}\,(0) + 2\eta_R\Omega\right] g_x(x) \end{aligned} \tag{S26}$$

Note: for the lower surface, where the normal points downwards, the sign of the surface tension term is reversed to maintain the right relation of curvature to normal direction.

6.5.2.3 Linearized kinematic boundary condition The linearized kinematic boundary condition is given by:

$$g_t + \bar{u}(0)\, g_x = \tilde{v}(x,0) \tag{S27}$$

6.5.3 Solution

To solve Eqs. (S26, S27, S28) we make use of Fourier transforms in the x direction to take advantage of translational invariance.

6.5.3.1 Solution of the linearized bulk equations Taking the Fourier transform in x:

$$\bar{\eta}\left(\partial_{yy} - k^2\right)\tilde{\mathbf{u}} - \Gamma_u \tilde{\mathbf{u}} - (ik, \partial_y)\, q = \mathbf{0} \quad \text{and} \quad (ik, \partial_y) \cdot \tilde{\mathbf{u}} = 0$$

Using that $\left(\partial_{yy} - k^2\right) q = 0$ we obtain:

$$\begin{aligned}
q &= A^+ e^{|k|y} + A^- e^{-|k|y} \\
\tilde{u} &= -\frac{ik}{\bar{\eta}}\delta^2\left(\mu_k^{\pm} A\right) + \left(\mu_\star^{\pm} B\right) \\
\tilde{v} &= -\frac{|k|}{\bar{\eta}}\delta^2\left(\Delta_k^{\pm} A\right) - \frac{ik}{|\star|}\left(\Delta_\star^{\pm} B\right) \\
\tilde{u}_y &= -\frac{ik\,|k|}{\bar{\eta}}\delta^2\left(\Delta_k^{\pm} A\right) + |\star|\left(\Delta_\star^{\pm} B\right) \\
\tilde{v}_y &= -\frac{|k|^2}{\bar{\eta}}\delta^2\left(\mu_k^{\pm} A\right) - ik\left(\mu_\star^{\pm} B\right)
\end{aligned} \tag{S28}$$

Where $\star^2 = k^2 + \delta^{-2}$ and $\mu_k^{\pm} f = e^{\pm|k|H} f^+ + e^{\mp|k|H} f^-$ and $\Delta_k^{\pm} f = e^{\pm|k|H} f^+ - e^{\mp|k|H} f^-$. The coefficients $A^{\pm}$ and $B^{\pm}$ are to be determined from the boundary conditions.

6.5.3.2 Application of the stress boundary conditions Inserting Eq. (S28) into the linearized stress boundary conditions Eq. (S26) yields:

$$\begin{aligned}
-2ik\,|k|\,\delta^2 \frac{\eta}{\bar{\eta}}\left(\Delta^{\pm} A\right) + \frac{1}{|\star|}\left[2\eta k^2 + \bar{\eta}\delta^{-2}\right]\left(\Delta_\star^{\pm} B\right) + 2\frac{\eta_o}{\bar{\eta}} k^2 \delta^2\left(\mu^{\pm} A\right) + 2ik\eta_o\left(\mu_\star^{\pm} B\right) \\
= \left[\pm\eta_R \frac{2\Omega}{\delta}\tanh\left(\frac{H}{\delta}\right) + i2k\eta_o\frac{\eta_R}{\bar{\eta}}\Omega\right] g^{\pm}
\end{aligned}$$

and

$$\begin{aligned}
\left[1 + 2\frac{\eta}{\bar{\eta}}|k|^2\delta^2\right]\left(\mu^{\pm} A\right) + 2ik\eta\left(\mu_\star^{\pm} B\right) - 2i\frac{\eta_o}{\bar{\eta}} k|k|\delta^2\left(\Delta^{\pm} A\right) + 2\eta_o\frac{k^2}{|\star|}\eta\left(\Delta_\star^{\pm} B\right) \\
= \left(\pm\gamma k^2 + i2k\frac{\eta\eta_R}{\bar{\eta}} 2\Omega\right) g^{\pm}
\end{aligned}$$

which is a set of four linear equations for the four unknowns $A^{\pm}, B^{\pm}$ in terms of the top and bottom surface perturbations $g^{\pm}$. A very tedious calculation which we suppress here to maintain excitement yields an inversion of these relations.

6.5.3.3 Application of the kinematic boundary condition Combining this with the kinematic boundary condition:

$$g_t^{\pm} + ik\bar{u}^{\pm} g^{\pm} = \tilde{v}^{\pm}$$

and substituting $\tilde{v}^{\pm}$ we have:

$$\begin{aligned}
g_t^+ - ikUg^+ &= -\frac{|k|}{\bar{\eta}}\delta^2\Delta_k^+ A - \frac{ik|}{|\star|}\Delta_\star^+ B \\
g_t^- + ikUg^- &= -\frac{|k|}{\bar{\eta}}\delta^2\Delta_k^- A - \frac{ik|}{|\star|}\Delta_\star^- B
\end{aligned}$$

These equations can be solved to yield the evolution of the surface of a perturbed slab of finite width. Explicit analytical computation of these modes becomes tedious at this point.

6.5.4 Visualization and asymptotics

The evolution of the surface corresponding to a sinusoidal perturbation of the height $g \sim \mathrm{Re}\left[e^{ikx}\right]$ is given by $g \sim \mathrm{Re}\left[e^{i(kx+\omega t)}e^{-\alpha t}\right]$ where $i\omega - \alpha = \sigma$, the eigenvalue of the linearized coupled evolution equations. There are, generally, two eigenvalues and associated eigenvectors. The real part of the eigenvalues $\alpha(k)$ indicates whether the wave amplitude decreases, remains the same, or grows exponentially in time.

In general, we find that for thick slabs ($|kH| \gg 1$, $H \gg \delta$), the eigenvalues and eigenvectors correspond to two copies of the semi-infinite slab problem, with damped surface waves on the bottom surface propagating in a direction opposite to those on the top surface. For thin slabs ($H \leq \delta$) we find unstable modes, whose growth rate is reduced by both surface tension and Hall viscosity.

Since the algebra can get quite tedious, we present our results by first considering the problem in the absence of Hall viscosity and subsequently considering the changes brought about by the presence of Hall viscosity. In the absence of Hall viscosity, substituting the solutions for $A^{\pm}, B^{\pm}$ in terms of Δg and μg give evolution equations of the form:

$$\begin{bmatrix} \Delta g_t \\ \mu g_t \end{bmatrix} = \mathbf{M}_k \begin{bmatrix} \Delta g \\ \mu g \end{bmatrix} = \begin{bmatrix} \gamma a_\Delta & i2\Omega b_\mu \\ i2\Omega b_\Delta & \gamma a_\mu \end{bmatrix} \begin{bmatrix} \Delta g \\ \mu g \end{bmatrix} \tag{S29}$$

The dispersion relation and stability diagrams follow from the eigenvalues of $\mathbf{M}_k$. The coefficients $a_{\Delta,\mu}$ and $b_{\Delta,\mu}$ are complicated, but real, functions of the system parameters and wavenumber k, except for the surface tension γ and the (forcing) spinning frequency 2Ω which appears only multiplicatively in $\mathbf{M}_k$ as shown. Hence, in the absence of surface tension the eigenvalues of $\mathbf{M}_k$ are either a purely imaginary, complex conjugate pair, or a real-valued positive/negative pair.

Regions of stability and instability are depicted in Figure S15c in the limit of vanishing surface tension and in Figure S16c for finite surface tension.

6.5.4.1 Intermediate surface waves For finite wavenumber $k\delta$, above a certain thickness $2H$, the eigenvalues correspond to propagating waves that are damped in the presence of surface tension. A representative dispersion $\omega(k)$ relation and damping rate α for the waves are depicted in Figures S15b and S16b. The corresponding flow fields are depicted in Figures S15a and S16a. The two eigenvalues correspond in this case to surface waves that propagate to the left in on the top surface and to the right on the bottom surface.

Taking the limit of large thickness $|kH| \gg 1$, and long wavelength $|k\delta| \ll 1$, and restricting our attention to the upper surface, we find the following asymptotic expression:

$$i\omega + \alpha = 2iu_{\mathrm{edge}}\frac{\eta}{\Gamma_u}k^3 + \frac{\gamma}{\Gamma_u}|k|^3$$

which corresponds to waves moving in the same direction as u_{edge}, damped by surface tension.

This reflects the intuitive expectation that for $H \gg \delta$ the problem should reduce to two copies of the semi-infinite slab problem. Adding Hall viscosity, computing the finite slab spectrum numerically and comparing it to the semi-infinite slab problem with Hall viscosity further confirms this intuition.

6.5.4.2 Short waves For finite thickness, and sufficiently large wavenumber $k\delta \gg 1$, $kH \gg 1$, Eq. (S29) simplify to

$$\begin{bmatrix} \Delta g_t \\ \mu g_t \end{bmatrix} = \begin{bmatrix} -\tilde{\gamma}|k| & i2\frac{\eta_R}{\bar{\eta}}\delta\Omega\tanh\left(\frac{\bar{h}}{\delta}\right)|k| \\ i2\frac{\eta_R}{\bar{\eta}}\delta\Omega\tanh\left(\frac{\bar{h}}{\delta}\right)|k| & -\tilde{\gamma}|k| \end{bmatrix} \begin{bmatrix} \Delta g \\ \mu g \end{bmatrix} \tag{S30}$$

with $\tilde{\gamma} = \frac{\gamma}{2\eta_R\left(2-\frac{\eta}{\bar{\eta}}\right)} > 0$. Seeking exponential solutions $(\Delta g, \mu g) = e^{\sigma t}(\Delta g_0, \mu g_0)$ yields

$$\sigma = -\tilde{\gamma}|k| \pm i\frac{\eta_R}{\bar{\eta}}\delta 2\Omega\tanh\left(\frac{\bar{h}}{\delta}\right)|k|$$

Hence, small length-scales are stabilized by surface tension in a manner consistent with classical results for the two-dimensional Stokes equations [21] while the gyroscopic drive produces waves.

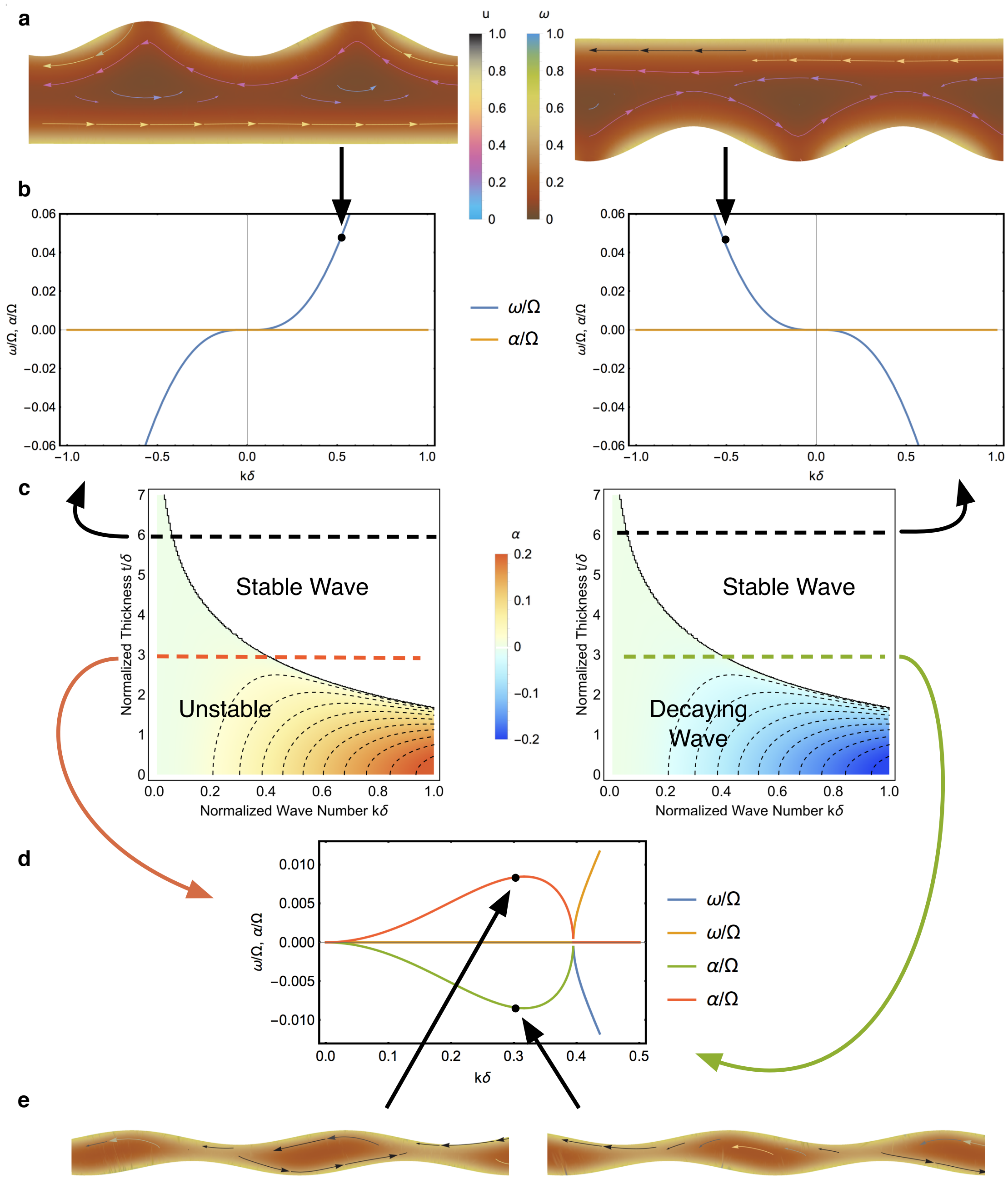

Supplementary Figure S15: **The nature of solutions to the linearized slab dynamics, in the absence of surface tension and Hall viscosity.** (a) Flow fields for the two branches of dispersive surface waves on a large thickness slab. (b) The dispersion relation (blue) and growth/decay rate for these surface waves. While difficult to discern due to its small magnitude, the latter is nonzero (positive at left, negative at right) near $k = 0$. (c) Stability diagram, showing the growth (red) or decay (blue) rates, as a function of normalized wavenumber and slab thickness. Stable waves are purely dispersive, having zero linear growth rate. Contours are levels of constant growth/decay rate. (d) The growth (red) and decay (green) rates, as a function of normalized wavenumber, for the unstable/stable modes on a slab. (e) The associated flow fields, and surface deformations, for the unstable (left) and stable (right) modes.

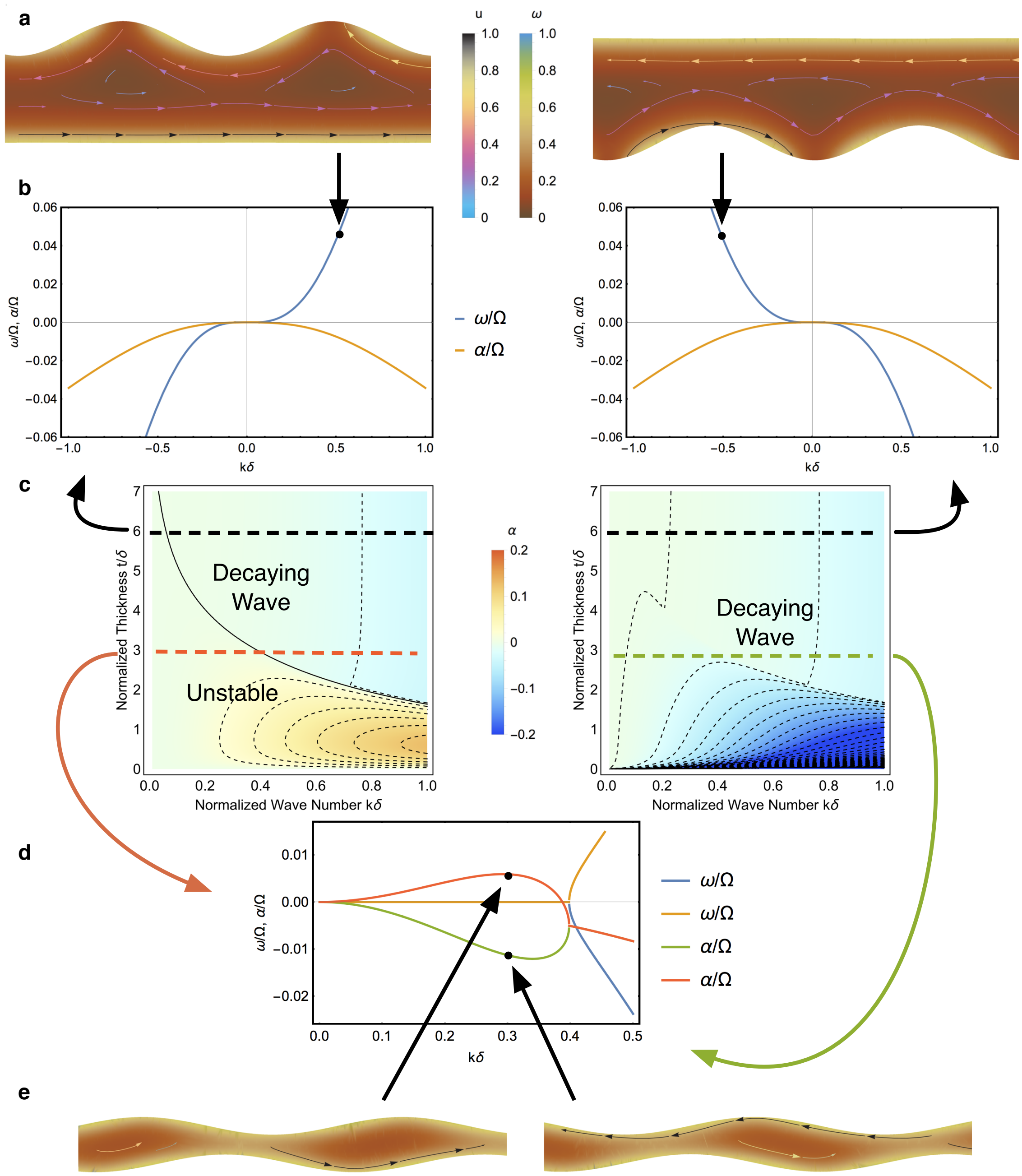

Supplementary Figure S16: **The nature of solutions to the linearized slab dynamics, in the presence of surface tension (in the absence of Hall viscosity).** (a) Flow fields for the two branches of damped, dispersive surface waves on a large thickness slab. (b) The dispersion relation (blue) and decay rates (red) for such surface waves. (c) Stability diagram, showing the growth (shades of red) or decay (shades of blue) rates, as a function of normalized wavenumber and slab thickness. Contours are levels of constant growth/decay rate. (d) The growth (red) and decay (green) rates, as a function of normalized wavenumber, for the unstable/stable modes on an unstable slab. (e) The associated flow fields, and surface deformations, for the unstable (left) and stable (right) modes.

6.5.4.3 Unstable long-wavelength modes For finite thickness slabs, $\eta_o = 0$, and long waves, $|k|H <<$ 1, one of the eigenvalues is always unstable, as can be seen in Figures S15c and S16c. Representative dependences on wavenumber of the growth/decay rates of the eigenvalues in this regime are shown in Figures S15d and S16d, together with the corresponding flow fields (Figures S15e and S16e). In this limit, Eq. (S29) simplify to

$$\begin{bmatrix} \Delta g_t \\ \mu g_t \end{bmatrix} = \begin{bmatrix} -\gamma\beta_1 k^4 & i2\Omega\alpha_1 k^3 \\ -i2\Omega\alpha_2 k & -\gamma\beta_2 k^2 \end{bmatrix} \begin{bmatrix} \Delta g \\ \mu g \end{bmatrix}$$

where $\beta_1 = H\delta^2/\bar{\eta}$, $\beta_2 = \delta^2/\bar{\eta}H$, $\alpha_1 = 2\delta^3 \left(\eta\eta_R/\bar{\eta}^2\right) \tanh\left(\frac{H}{\delta}\right)$, and $\alpha_2 = \left(2\delta^2/H\right)\left(\eta\eta_R/\bar{\eta}^2\right) \operatorname{sech}^2\left(\frac{H}{\delta}\right)$ are all positive constants. Seeking exponential solutions $(\Delta g, \mu g) = e^{\sigma t}(\Delta g_0, \mu g_0)$ yields

$$\sigma = \frac{1}{2}\left[-\gamma\beta_2 \pm \left((\gamma\beta_2)^2 + 2\Omega^2\alpha_1\alpha_2\right)^{1/2}\right] k^2 \tag{S31}$$

Hence, at long wavelengths, there is always both a stable and an unstable mode. In each case, both surface tension and driving scale quadratically in k in the eigenvalue, and surface tension damps both stable and unstable modes generated by activity (i.e. $2\Omega^2 > 0$).

Performing the same calculation numerically in the presence of Hall viscosity presents a similar picture. Hall viscosity, like surface tension, generally acts as a stabilizing stress, albeit with a different wavenumber dependence, as illustrated in Figure S17.

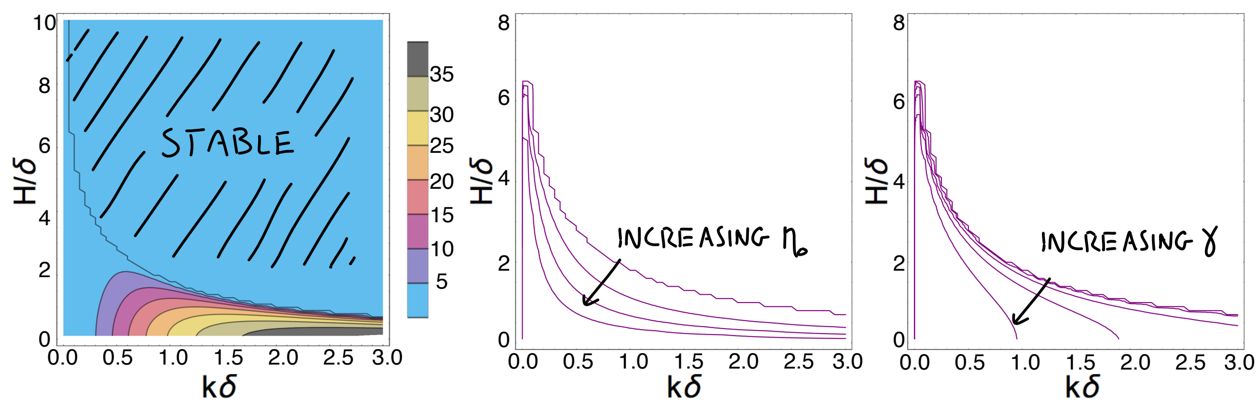

Supplementary Figure S17: **Effect of surface tension and Hall viscosity on the stability of finite thickness slabs.** (a) The stability diagram in the absence of surface tension and Hall viscosity (c.f. Figure S15). (b) Increasing the Hall viscosity, η_o, moves the line separating stable from unstable modes as depicted. (c) Increasing the surface tension, γ, moves the line separating stable from unstable modes as depicted. In both cases the effect is to stabilize the interface by increasing the extent of the stable region. The large wavenumber dependence of the damping effects of surface tension and Hall viscosity accounts for the different effects they have on the stability diagram.

6.6 Perturbation of droplet flow

To compute the surface modes of a circular droplet of chiral fluid, we followed a procedure similar to the one described above for the semi-infinite and finite slab flows. We defer details to a future publication but state the result here.

6.6.1 Solution and visualization

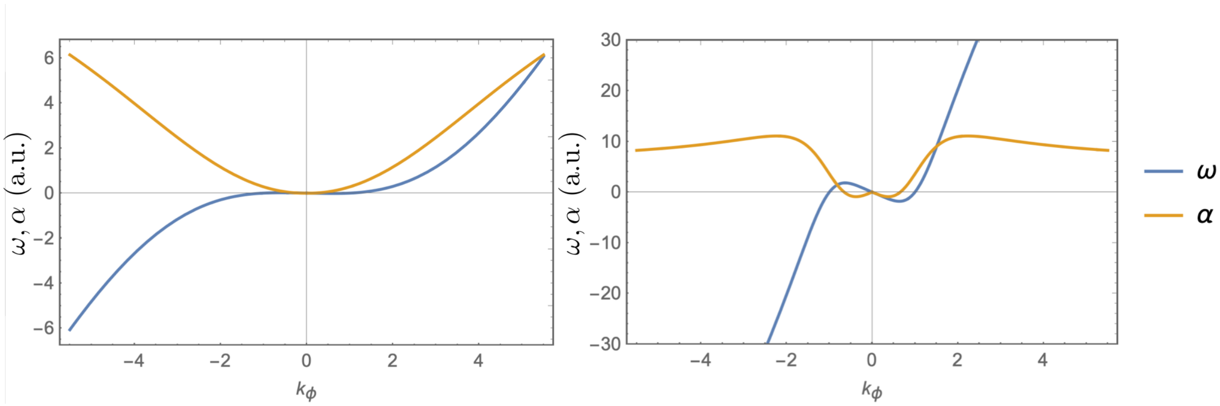

Supplementary Figure S18: **Surface wave dispersion for perturbations of circular droplets.** (a) At $R/\delta \gg 1$ there is little change when compared to the semi-infinite slab problem. (b) For $R/\delta \sim 1$ the effects of finite radius become significant.

The spectrum $\omega(k_\phi)$ and dissipation rate $\alpha(k_\phi)$ of surface waves on circular droplets can be obtained as a function of the dimensionless azimuthal wavenumber k_ϕ by solving

$$\begin{aligned} i(\omega + i\alpha)\bar{R} &= -ik_\phi \delta \Omega \frac{\eta_R I_1\left(\frac{\bar{R}}{\delta}\right)}{\eta I_2\left(\frac{\bar{R}}{\delta}\right) + \eta_R I_0\left(\frac{\bar{R}}{\delta}\right)} \\ &\quad - |k_\phi \delta| \frac{\delta}{\bar{R}} \bar{R}^{|k_\phi|} \frac{1}{\eta + \eta_R} \frac{\beta_2 \rho_1 - \beta_1 \rho_2}{\alpha_1 \beta_2 - \beta_1 \alpha_2} \\ &\quad + \frac{1}{2ik_\phi}\left(I_{|k|+1}\left(\frac{\bar{R}}{\delta}\right) - I_{|k|-1}\left(\frac{\bar{R}}{\delta}\right)\right) \frac{\alpha_1 \rho_2 - \alpha_2 \rho_1}{\alpha_1 \beta_2 - \beta_1 \alpha_2}, \end{aligned}$$

where I_k are the modified Bessel functions of the first kind and:

$$\rho_1 = -\frac{\gamma}{\bar{R}}(k_\phi^2 - 1) - 2\Omega(\eta_o - ik_\phi \eta) \frac{\eta_R I_2\left(\frac{\bar{R}}{\delta}\right)}{\eta I_2\left(\frac{\bar{R}}{\delta}\right) + \eta_R I_0\left(\frac{\bar{R}}{\delta}\right)}$$

$$\rho_2 = -2ik\eta_o \Omega \frac{\delta}{\bar{R}} \frac{\eta_R I_1\left(\frac{\bar{R}}{\delta}\right)}{\eta I_2\left(\frac{\bar{R}}{\delta}\right) + \eta_R I_0\left(\frac{\bar{R}}{\delta}\right)} + 2\Omega\eta \frac{\eta_R I_2\left(\frac{\bar{R}}{\delta}\right)}{\eta I_2\left(\frac{\bar{R}}{\delta}\right) + \eta_R I_0\left(\frac{\bar{R}}{\delta}\right)} - (\eta + \eta_R)\Omega \frac{\bar{R}}{\delta} \frac{\eta_R I_1\left(\frac{\bar{R}}{\delta}\right)}{\eta I_2\left(\frac{\bar{R}}{\delta}\right) + \eta_R I_0\left(\frac{\bar{R}}{\delta}\right)}$$

$$\alpha_1 = -\bar{R}^{|k_\phi|}\left[1 + \frac{2}{(\eta + \eta_R)} \frac{\delta^2}{\bar{R}^2}(|k_\phi| - 1)(\eta |k_\phi| - i\eta_o k_\phi)\right]$$

$$\alpha_2 = -\frac{\delta^2}{\bar{R}^2} \bar{R}^{|k_\phi|} \frac{2}{(\eta + \eta_R)}(|k_\phi| - 1)(\eta_o |k_\phi| + i\eta k_\phi)$$

$$
\begin{aligned}
\beta_1 &= i\frac{\eta}{k_\phi \bar{R}}\left[(|k_\phi|-1)I_{|k|-1}\left(\frac{\bar{R}}{\delta}\right)+(|k_\phi|+1)I_{|k|+1}\left(\frac{\bar{R}}{\delta}\right)\right] \\
&\quad +\frac{\eta_o}{|k_\phi|\bar{R}}\left[(|k_\phi|-1)I_{|k|-1}\left(\frac{\bar{R}}{\delta}\right)-(|k_\phi|+1)I_{|k|+1}\left(\frac{\bar{R}}{\delta}\right)\right]
\end{aligned}
$$

$$
\begin{aligned}
\beta_2 &= -\frac{\eta+\eta_R}{|k_\phi|\delta}I_{|k|}\left(\frac{\bar{R}}{\delta}\right) \\
&\quad +\frac{\eta}{|k_\phi|\bar{R}}\left[(|k_\phi|+1)I_{|k|+1}\left(\frac{\bar{R}}{\delta}\right)-(|k_\phi|-1)I_{|k|-1}\left(\frac{\bar{R}}{\delta}\right)\right] \\
&\quad +i\frac{\eta_o}{k_\phi\bar{R}}\left[(|k_\phi|+1)I_{|k|+1}\left(\frac{\bar{R}}{\delta}\right)+(|k_\phi|-1)I_{|k|-1}\left(\frac{\bar{R}}{\delta}\right)\right]
\end{aligned}
$$

and $\bar{R}$ is the unperturbed droplet radius. Representative plots of the resulting $\omega(k_\phi)$ and $\alpha(k_\phi)$ are shown in Figure S18.

6.7 Physical interpretation of dynamics

We examine the roles of surface tension, shear viscosity, Hall viscosity and rotational viscosity in determining the surface dynamics of the chiral fluid.

6.7.1 Surface waves driven by "edge pumping"

We begin by considering the propagation of waves in the limit $\eta_o = \gamma = 0,\ \eta_R \neq 0,\ \eta \to 0$. In this limit, the surface waves are undamped ($\alpha(k) = 0$). The asymptotic dispersion relation computed in Section 6.4 for a semi-infinite slab:

$$
\omega(k) = \begin{cases} 2u_{\text{edge}}\dfrac{\eta}{\Gamma_u}k^3 & |k\delta| \ll 1 \\ -\dfrac{2\eta_R\Omega}{\eta+2\eta_R} + u_{\text{edge}}k & |k\delta| \gg 1 \end{cases}
$$

provides a basis for discussion. The dispersion relation suggests that in the limit $\eta \to 0$, surface dynamics might be suppressed. This is indeed the case!

Consider the limit $\eta = \eta_o = 0$. The stress boundary condition, Eq. (S12), reduces simply to $p|_{\partial D} = 0$ and $\omega|_{\partial D} = 2\Omega$. Since $\nabla^2 p = 0$ we have $p \equiv 0$ and, hence, $\nabla p \equiv 0$. This reduces the bulk flow equations to

$$
\mathbf{u} = \frac{\eta_R}{\Gamma_u}\left(-\partial_y\omega, \partial_x\omega\right). \tag{S32}
$$

Evaluating this expression on the boundary ∂D, contracting it against the normal, and applying the kinematic boundary condition yields

$$
\mathbf{v}\cdot\mathbf{n} = \frac{v_s}{\Gamma_u}\frac{\partial}{\partial s}\omega|_{\partial D} \equiv 0
$$

where the last equality uses that ω is constant on the boundary. Hence, the normal velocity of the boundary is zero, and ∂D is static.

Lack of surface dynamics does not imply a lack of edge flow; Indeed, Eq. (S32) establishes a direct connection between a gradient in vorticity and transverse flow. As already noted, the vorticity satisfies the screened Laplace equation:

$$
\left(\nabla^2 - \frac{1}{\delta^2}\right)\omega = 0
$$

with the boundary condition $\omega = 2\Omega_0$ (for $\eta = \eta_o = 0$). Vorticity at the surface is thus screened on the interior, with the value dropping to zero at distances of a few δ from the boundary. Eq. (S32) implies that a gradient of vorticity corresponds to flow perpendicular to the gradient, thus the fluid flows along the equi-vorticity lines. Since the vorticity deep in the fluid is zero, the total mass flux of the edge current – obtained by integrating the gradient of the vorticity along a line from the interior of the chiral fluid to its surface – is

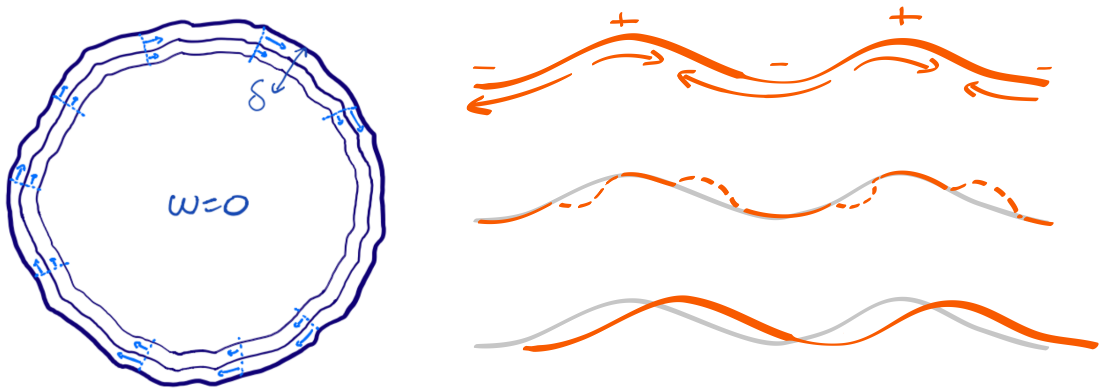

Supplementary Figure S19: **The edge-pumping effect**. (Left:) in the absence of viscosity and surface tension, the boundaries of our chiral fluid droplets do not move; they simply have an exponentially screened edge current glued to them. (Right:) In the presence of viscosity, differential mass flux in the edge current shifts fluid from one region to another, which in the case of a sinusoidal perturbation results in wave propagation.

proportional to the value of the vorticity at the surface. In the absence of viscosity η and Hall viscosity η_o, the latter is constant and the mass flux is constant at all points along the surface. *Thus in the absence of viscosity (and surface tension), the boundary of our chiral fluid droplets does not move, and simply has an exponentially screened edge current glued to it.*

In the presence of viscosity η, however, the value of vorticity at the surface will be increased (decreased) in positively (negatively) curved regions of the boundary, giving rise to enhanced (reduced) mass flux in response to reduced (increased) viscous drag. The differential mass flux then effectively pumps fluid from one region of the surface to another, giving rise to dynamics. A sketch of the resulting flow in the case of a sinusoidal perturbation is shown in Figure S19. In this case the result is wave propagation. *This "edge-pumping" effect is the fundamental mechanism that gives rise to free surface dynamics of our chiral fluids.*

Sidenote 1: We note that an analogy can be made between vorticity in our system and the electric potential inside a conducting medium, with penetration depth δ. The velocity at the edge depends on the curvature of the surface, roughly as $|\mathbf{u}| = (1 + C\kappa)2\Omega\delta$ for small curvature κ; in the electrostatic analogy, the latter is proportional in magnitude to the surface charge on the conductor which in turn depends on the curvature of the surface. Crucially then, the mass flux in this tangential surface flow is determined by the vorticity ω on the surface: integrating $\frac{\eta_R}{\Gamma_u}\nabla\omega$ from the center (where $\omega = 0$) to the edge is at once equal to $(\eta_R/\Gamma_u)2\Omega$, and hence proportional to the value of the vorticity at the boundary, and equal to the total mass flux.

Sidenote 2: For nonzero surface tension (and zero Hall viscosity), it is straightforward to show that the surface dynamics when $\eta = 0$ is curve-shortening. Consider a droplet of chiral fluid whose boundary length is $L(t)$. A standard equality is then $\dot{L} = \int_{\partial D} ds\kappa\, \mathbf{v}\cdot\mathbf{n}$. Using the bulk flow equation and that $\omega_s = 0$ on the boundary yields

$$\dot{L} = -\frac{1}{\gamma\Gamma_u}\int_{\partial D} ds\; p\,\frac{\partial p}{\partial \mathbf{n}} = -\frac{1}{\gamma\Gamma_u}\int_D dA\; |\nabla p|^2 < 0 \tag{S33}$$

where in the last identity we used the divergence theorem and that p is harmonic. Hence, the long-time behavior is simply relaxation to a circular drop.

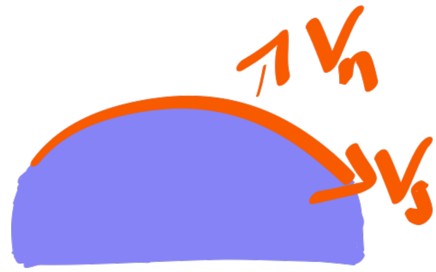

Supplementary Figure S20: **The tangential and normal components of velocity at the boundary** give rise to a normal Hall stress $\eta_o \left(\partial_s v_n + \frac{v_s}{R}\right)$

6.7.2 Effects of Hall stress

For an incompressible fluid, the Hall viscosity has no effect on bulk flows. Its influence is instead felt on the boundary where it exerts a stress whose normal component is

$$\sigma^o_{nn} = \eta_o \left(\partial_s v_n + \frac{v_s}{R}\right)$$

Here, v_s and v_n are the tangential and normal components of velocity, as shown Figure S20. Note that in the absence of odd stress η_R and drive, or surface tension γ, there is no flow at the surface and Hall viscosity has no effect.

6.7.3 Hall damping

The presence of Hall viscosity does not affect surface dynamics in the absence of both surface tension and odd stress, as the Hall surface stress is proportional to the surface flow. Thus the effect that Hall viscosity has on both the propagation and damping of waves originates from the combined effect of Hall viscosity and surface tension, or Hall viscosity and the localized edge current glued to the boundary of our fluid.

In the absence of surface tension, but in the presence of odd stress, the damping of surface waves on a semi-infinite slab $\alpha(k)$ is given by:

$$\alpha(k) = \begin{cases} \dfrac{2\eta_o u_{\text{edge}}}{\Gamma_u}|k|^3 & |k\delta| \ll 1 \\ \dfrac{2\eta_o\eta_R\Omega}{(\eta+2\eta_R)^2+\eta_o^2} & |k\delta| \gg 1 \end{cases}$$

This damping originates from the normal component to the boundary Hall stress $\frac{\eta_o u_{\text{edge}}}{R}$, where R is the radius of curvature of the surface. This stress has identical form to the stress arising from surface tension and thus acts to reduce the curvature of the interface (see Figure S21).

Dimensionally, for long waves (small wavenumbers compared to δ), a competition of Hall surface stress and substrate friction:

$$\left[\frac{\eta_o u_{\text{edge}}}{\Gamma_u}\right] \sim \frac{L^3}{T}$$

suggests a scaling with k^3 as found by the calculation above. For short waves however (large wavenumber compared to δ), the substrate friction is no longer relevant and the relevant quantities (in the absence of surface tension) are: $\eta_o, \eta_R, \eta, \Gamma, \Omega, k$. These have dimensions:

$$[\eta_o] = [\eta_R] = [\eta] = \frac{M}{T}, \qquad [\Omega] = \frac{1}{T}, \qquad [k] = \frac{1}{L}$$

Supplementary Figure S21: **Hall tension.** The edge current induces a Hall stress that acts like surface tension to flatten the interface.

Since the viscosities η_o, η_R, η must appear as ratios, the only quantity with the required units of T^{-1} is Ω and the wavenumber k drops out of the problem. This is in contrast to the case of surface tension where the units of length associated with the surface tension $[\gamma] = ML/T^2$ give rise to a linear wavenumber dependence.

These surface stresses lead to the exponential decay of surface perturbations. This role of Hall stress in the damping of surface waves may seem unusual as Hall viscosity is a transverse, conservative stress. This arises in our case from the over-damped nature of our dynamics.

6.7.4 Capillary Hall waves

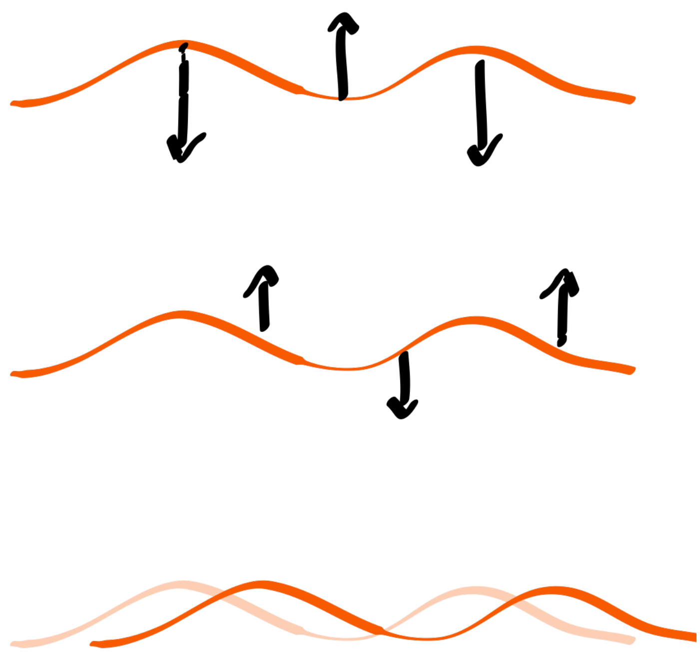

Supplementary Figure S22: **Capillary-Hall mechanism.** Surface tension induces a flattening of the interface which the Hall stress $\eta_0 \partial_s v_n$ converts into wave propagation.

For a sinusoidal perturbation to the surface height $h \sim \cos(kx)$, we expect surface tension to drive an in-phase flattening flow $v_n \propto \cos(kx)$. This results in an out-of-phase Hall stress $\eta_o \partial_s v_n \sim \eta_o \sin(kx)$ which acts on the inflection points of the sinusoidal perturbation. The result is uni-directional propagation of the sinusoidal perturbation (see Figure S22). These waves are in turn damped by surface tension:

$$\alpha(k) = \begin{cases} \dfrac{\gamma}{\Gamma_u}|k|^3 & |k\delta| \ll 1 \\ \dfrac{1}{2}\dfrac{\gamma\eta}{\eta^2+\eta_o^2}\ |k| & |k\delta| \gg 1 \end{cases}$$

In the absence of u_{edge}, and thus of the edge-pumping mechanism, waves can still propagate, as evidenced by the dispersion relation for waves on a semi-infinite slab (with $\gamma = \eta_R = 0$):

$$\omega(k) = \begin{cases} 4\dfrac{\gamma\eta_o}{\Gamma_u^2}\ k^5 & |k\delta| \ll 1 \\ \dfrac{1}{2}\dfrac{\gamma\eta_o}{\eta^2+\eta_o^2}\ k & |k\delta| \gg 1 \end{cases}$$

Both the drive and damping in this case come from a combination of surface tension γ and Hall viscosity η_o. The mechanism giving rise to these uni-directional waves can be understood in simple terms from the contribution to the normal component to the boundary Hall stress: $\eta_o \partial_s v_n$.

It would be interesting to consider this kind of capillary-Hall waves as a feature of under-damped interfaces as well.

6.7.5 Effects of finite odd substrate friction

In the calculation of Section 6.4, we neglected the transverse component $\Gamma_\perp$ of the substrate friction tensor Γ_{ij}, as a measurement of the substrate friction (Section 3.1) excluded the contribution of transverse friction to the observed dynamics. In this section, we investigate the effect that a finite $\Gamma_\perp$ would have on the surface dynamics of our chiral fluid. We find that transverse friction introduces corrections to the dispersion $\omega(k)$ and dissipation rate $\alpha(k)$ of surface waves. For long wavelengths, the contribution to $\alpha(k)$ from $\Gamma_\perp$ resembles that of surface tension γ and odd viscosity η_o; at short wavelengths, however, the contribution of $\Gamma_\perp$ drops off, unlike γ and η_o.

Repeating the calculation of Section 6.4 for finite $\Gamma_\perp$, we obtain the dispersion $\omega(k)$ and dissipation rate $\alpha(k)$ plotted in Figure S23a. From this result we can extract the corrections, to leading order in k, to the dispersion and dissipation rate due to transverse friction. In the long wavelength limit, $|k\delta| \ll 1$, the asymptotic dispersion and dissipation rates are:

$$\begin{aligned} \omega(k) &= -\gamma\frac{\Gamma_u\Gamma_\perp}{\bar{\Gamma}^3}\sqrt{\frac{\Gamma_u}{\bar{\Gamma}}}k^3 + \left(\frac{\Gamma_u}{\bar{\Gamma}}\frac{\eta}{\Gamma_u} - \frac{\Gamma_\perp}{\bar{\Gamma}}\frac{\eta_o}{\Gamma_u}\right)\frac{\Gamma_u}{\bar{\Gamma}}u_{\text{edge}}k^3, \\ \alpha(k) &= \gamma\frac{\Gamma_u^2}{\bar{\Gamma}^3}\sqrt{\frac{\Gamma_u}{\bar{\Gamma}}}|k|^3 + \left(\frac{\Gamma_\perp}{\bar{\Gamma}}\frac{\eta}{\Gamma_u} + \frac{\Gamma_u}{\bar{\Gamma}}\frac{\eta_o}{\Gamma_u}\right)\frac{\Gamma_u}{\bar{\Gamma}}u_{\text{edge}}|k|^3, \end{aligned}$$

where $\bar{\Gamma} = \sqrt{\Gamma_u^2 + \Gamma_\perp^2}$. By comparison to Section 6.4.4 and 6.7, we see that $\Gamma_\perp$ causes a rescaling of dispersive terms that originate from edge-pumping. Then, by comparison to Section 6.4.4 and 6.7.3, we see a similar rescaling of the dissipative terms that originate from surface tension and Hall stress. Further, $\Gamma_\perp$ introduces a correction to the long-wavelength dispersion due to both surface tension and Hall viscosity and an addition to the dissipation rate mediated by the shear viscosity η. The latter can be understood as illustrated in Figure S23b:

($\eta = 0$) Without shear viscosity the mass flux is constant, so the transverse friction generates a uniform pressure over the surface.

($\eta \neq 0$) Meanwhile, the presence of shear viscosity enables a differential mass flux (see Section 6.7) that couples the curvature to the dissipation rate, such that the transverse friction acts like a surface tension.

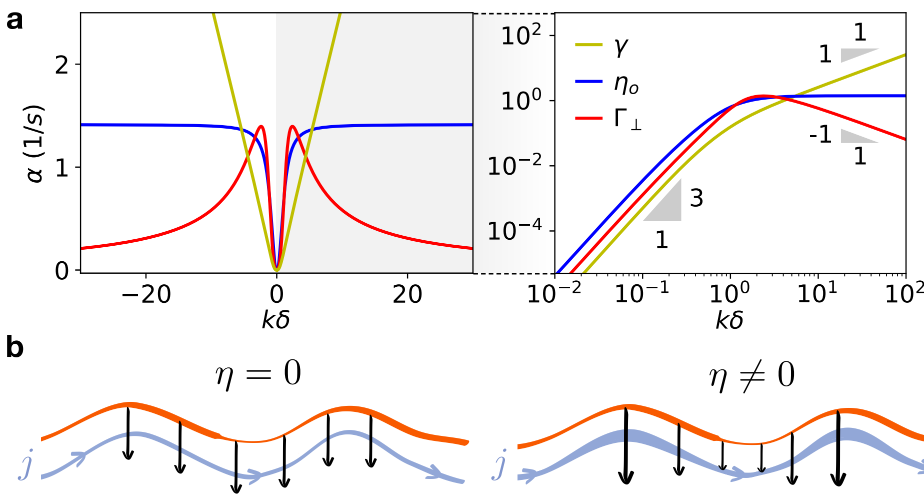

Supplementary Figure S23: **Wave damping due to transverse friction. a,** The wave damping associated with Hall viscosity η_o, transverse friction $\Gamma_\perp$, and surface tension γ scales as $|k|^3$ for $|k\delta| \ll 1$. However, at $|k\delta| \gg 1$, the damping rates scales as $|k|^0$, $|k|^{-1}$, and $|k|^1$ respectively. **b,** In the limit $|k\delta| \ll 1$, when $\eta \neq 0$, the mass flux j varies with curvature, so that the transverse friction acts like a surface tension. In the absence of a shear viscosity η, the mass flux at a free surface is constant, such that the force of transverse friction is to induce a constant pressure.

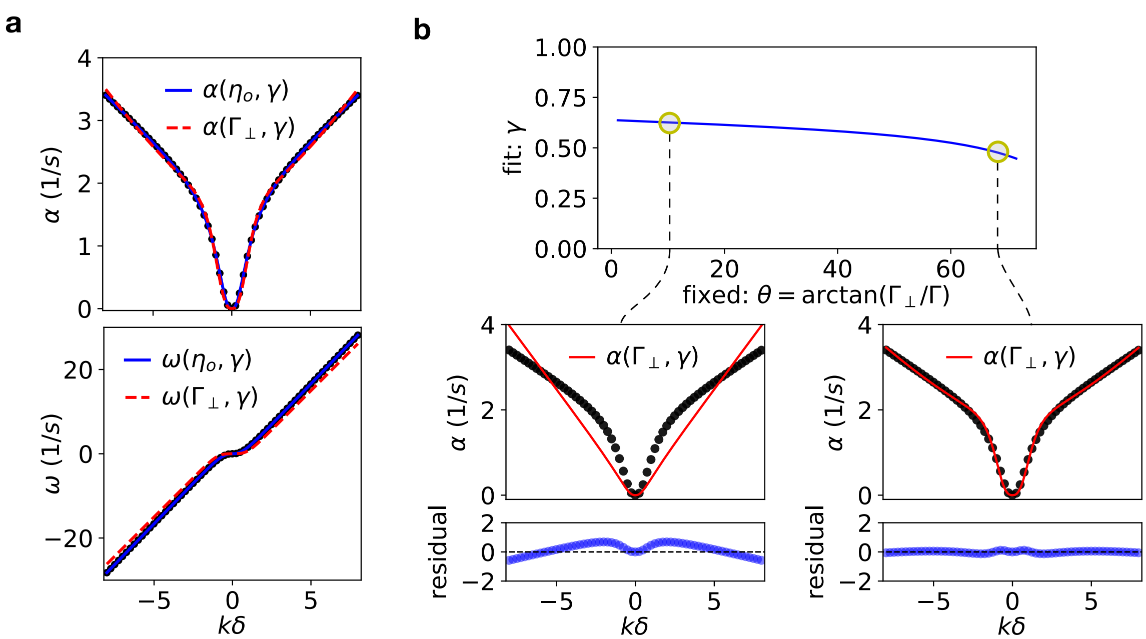

Supplementary Figure S24: **Disambiguating Hall viscosity and transverse friction. a,** The dissipation and dispersion measured in the low-friction experiments can be captured by the hydrodynamic theory in the limit $\eta_o = 0$ or $\Gamma_\perp = 0$, but **b,** $\Gamma_\perp/\Gamma_u$ must be large to permit this agreement.

Apparently, the dissipation rate due to Hall viscosity η_o, transverse friction $\Gamma_\perp$, and surface tension γ scales as $|k|^3$ for $|k\delta| \ll 1$.

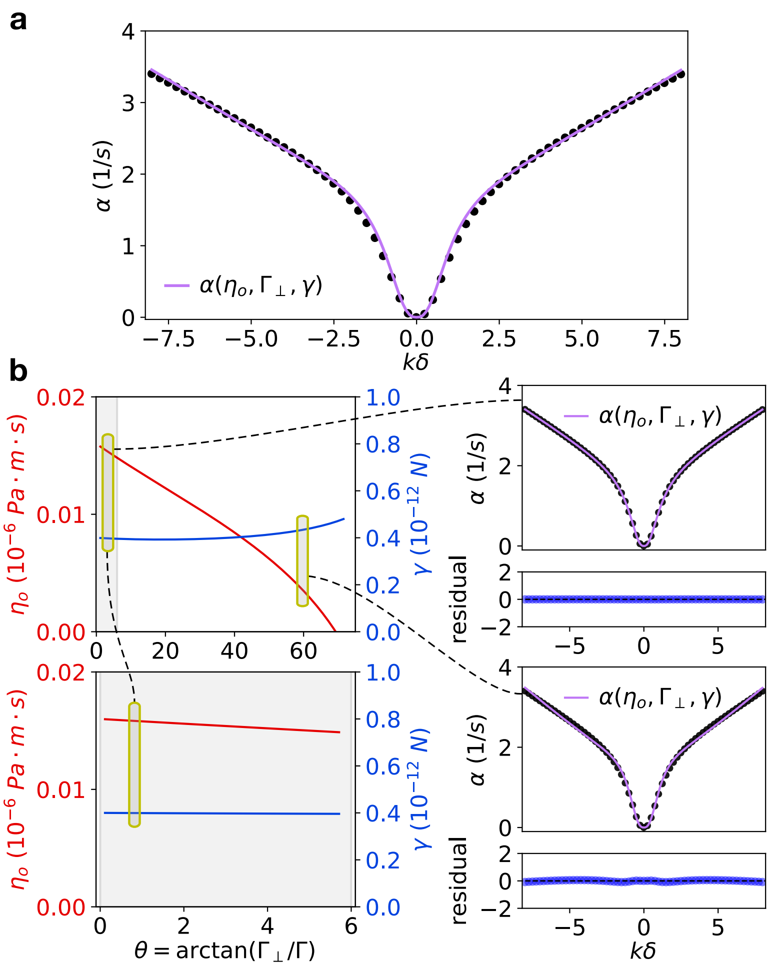

Supplementary Figure S25: **Transverse friction does not contribute to the dissipation rate. a,** The low-friction dissipation rate can be modelled by a theory including η_o and $\Gamma_\perp$, but the relative size of these coefficients is not uniquely determined. **b,** Fixing $\Gamma_\perp$ and fitting for η_o and γ demonstrates that $\Gamma_\perp$ and η_o can be interchanged to predict the dissipation, but in the physical limit ($\Gamma_\perp/\Gamma_u \ll 1$), Hall damping is the dominant contribution to the model.

In the short wavelength limit, $|k\delta| \gg 1$, the $\mathcal{O}(1)$ and $\mathcal{O}(k)$ contributions to the dispersion and dissipation rate (see Section 6.4.4) are unchanged. We find however for $\gamma = \eta_o = 0$, the correction to the dissipation is

$$\alpha(k) = \frac{\Gamma_\perp}{2\Gamma_u} \frac{\eta_R(\eta + \eta_R)\Omega}{\eta(\eta + 2\eta_R)} \frac{1}{|k\delta|},$$

such that the damping associated with transverse friction rapidly falls off for large $|k\delta|$. By contrast, the damping due to Hall viscosity is wavelength-independent in this limit, as illustrated in Figure S23a. As the effect of Hall viscosity and transverse friction arise as a transverse boundary stress, the qualitative similarity in damping behavior between η_o and $\Gamma_\perp$ up to intermediate $|k\delta|$ begs the question: to what extent can $\Gamma_\perp$ mimic the effects of η_o? In the following sections, we inspect the wave dissipation rate over a finite range of $k\delta$ and see that transverse friction could indeed mimic Hall viscosity. We show, however, that this potential ambiguity is eliminated by our measurement of transverse friction.

Modelling wave dissipation with transverse friction. We first investigate the possibility that finite $\Gamma_\perp$ and γ, in the absence of η_o might account for the dissipation rate measured within a finite range of $|k\delta| < 10$. Here, we find that this is indeed possible, but only for large values of $\Gamma_\perp/\Gamma_u$, which are ruled out by direct measurement of the friction coefficients in Section 3.1.

We proceed as in Figure 4d in which we fit the low-friction dissipation rate for Hall viscosity η_o and surface tension γ with $\Gamma_\perp = 0$. Now, consider the case $\eta_o = 0$ for finite values of $\Gamma_\perp$ and γ. Figure S24a shows that we find excellent agreement between this modified theory and the fit curve of Figure 4d, for $\Gamma_\perp/\Gamma_u \sim 2.6$ and $\gamma \sim 4.7 \times 10^{-13}$ N. We stress that this estimate of $\Gamma_\perp$ is, however, inconsistent with our sedimentation measurements (see Section 3.1) from which we showed that $\Gamma/\Gamma_\perp \ll 1$

To investigate the correlation between $\Gamma_\perp$ and γ, we fix the value of $\Gamma_\perp$ and fit the dissipation rate for γ. We repeat this procedure for values of $\Gamma_\perp/\Gamma_u$ in the range $(0.2, 3)$ and present our results in Figure S24b. The value of γ is not strongly effected by the value of $\Gamma_\perp$, and a large value of $\Gamma_\perp$ is required to produce a good fit. This demonstrates that the transverse friction must be large compared to the longitudinal friction to produce the hallmark features of Hall viscosity.

Interplay of Hall viscosity and transverse friction. In this section, we fit the theory curve of Figure 4d to a theory including η_o, $\Gamma_\perp$, and γ to investigate the interplay of Hall viscosity and transverse friction. We find that the dissipation rate can be fit well by such a comprehensive theory for $\eta_o \sim 8 \times 10^{-9}$ Pa m s, $\Gamma_\perp/\Gamma_u = 1$, and $\gamma \sim 4 \times 10^{-13}$ N, as in Figure S25a.

In this procedure, however, there is a high level of parameter uncertainty due to the overlap in qualitative behavior between the damping due to each parameter for $|k\delta| \ll 1$. With this in mind, we consider the problem of fitting the dissipation rate with a range of constrained transverse friction values. While the damping can be adequately captured for both small and large $\Gamma_\perp/\Gamma_u$, the relative role of η_o decreases with increasing $\Gamma_\perp$ (Figure S25b top). Using the physical reasoning of Section 3.1, which constrains $\theta = \arctan(\Gamma_\perp/\Gamma_u) \ll 1$, we find that the measurements of η_o and γ are largely unresponsive to the inclusion of $\Gamma_\perp$ (Figure S25b bottom). This demonstrates that the dominant contributions to the observed dissipation rate are surface tension γ and Hall viscosity η_o.

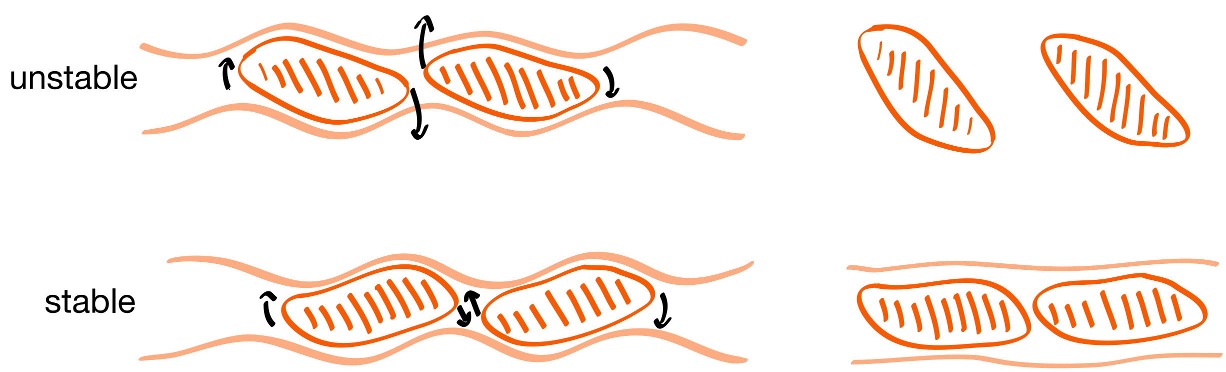

Supplementary Figure S26: Cartoon of the phase relations of the bounding interfaces of a chiral fluid slab that give rise to growth (upper) and decay (lower) of perturbations.

6.7.6 An odd hydrodynamic instability

Here we give a simple geometric model that explains the nature of the stable and unstable modes of the slab, the latter of which leads to the formation of droplets in experiment. Consider the coupled surface modes for the slab computed above (see Eqs. (S29, S31)). These consist of sinusoidal perturbations on the top and bottom surfaces, respectively, that have relative phases of either $\pi/2$ or $-\pi/2$, with their respective flow fields plotted in Figures S15e and S16e. In the unstable case the upper surface is shifted leftwards relative to the lower, and oppositely for the stable case. As depicted in Figure S26 the geometry of such a perturbed slab can be approximated by a collection of elongated droplets of chiral fluid, all canted in the same direction. In isolation, droplets of this kind would rotate clockwise. Because of their canted angle, the configuration shown in Figure S26 (top) would evolve into separate droplets, whereas that shown in Figure S26 (bottom) would evolve towards a flat slab-like configuration (stable). The former case is consistent with the reconstructed, unstable slab boundaries shown in Fig. 5b of the main text.

References

[1] Sugimoto, T., Sakata, K. & Muramatsu, A. Formation Mechanism of Monodisperse Pseudocubic $\alpha - Fe_2O_3$ Particles from Condensed Ferric Hydroxide Gel. *Journal of Colloid and Interface Science* **159**, 372–382 (1993).

[2] Rossi, L. *Colloidal superballs* (Utrecht University, 2012). OCLC: 6893354969.

[3] Cladé, P. PyDAQmx: a Python interface to the National Instruments DAQmx driver. URL `http://pythonhosted.org/PyDAQmx/`.

[4] Allan, Daniel and, Caswell, Thomas and, Keim, Nathan and & van der Wel, Casper. trackpy v0.3.2 (2016). URL `https://doi.org/10.5281/zenodo.60550`.

[5] Dahler, J. S. & Scriven, L. E. Theory of Structured Continua. I. General Consideration of Angular Momentum and Polarization. *Proceedings of the Royal Society of London A: Mathematical, Physical and Engineering Sciences* **275**, 504–527 (1963).

[6] Cowin, S. C. Polar Fluids. *The Physics of Fluids* **11**, 1919–1927 (1968).

[7] Brenner, H. & Nadim, A. The Lorentz reciprocal theorem for micropolar fluids. *Journal of Engineering Mathematics* **30**, 169–176 (1996).

[8] Tsai, J.-C., Ye, F., Rodriguez, J., Gollub, J. P. & Lubensky, T. C. A Chiral Granular Gas. *Physical Review Letters* **94**, 214301 (2005).

[9] Avron, J. E. Odd Viscosity. *Journal of Statistical Physics* **92**, 543–557 (1998).

[10] Avron, J. E., Seiler, R. & Zograf, P. G. Viscosity of Quantum Hall Fluids. *Physical Review Letters* **75**, 697–700 (1995).

[11] Wiegmann, P. & Abanov, A. G. Anomalous Hydrodynamics of Two-Dimensional Vortex Fluids. *Physical Review Letters* **113**, 034501 (2014).

[12] Banerjee, D., Souslov, A., Abanov, A. G. & Vitelli, V. Odd viscosity in chiral active fluids. *Nature Communications* **8**, 1573 (2017).

[13] Radin, S. Lorentz Plasma in a Strong Magnetic Field. *The Physics of Fluids* **15**, 91–95 (1972).

[14] Robinson, B. B. & Bernstein, I. B. A variational description of transport phenomena in a plasma. *Annals of Physics* **18**, 110–169 (1962).

[15] Pitaevskii, L. P. & Lifshitz, E. M. *Physical Kinetics* (Butterworth-Heinemann, Oxford, UK, 1981).

[16] Rossi, L. *et al.* Self-organization in dipolar cube fluids constrained by competing anisotropies. *Soft matter* **14**, 1080–1087 (2018).

[17] Krauß, R., Reimann, B., Richter, R., Rehberg, I. & Liu, M. Fluid pumped by magnetic stress. *Applied Physics Letters* **86**, 024102 (2005).

[18] Krauß, R., Liu, M., Reimann, B., Richter, R. & Rehberg, I. Pumping fluid by magnetic surface stress. *New Journal of Physics* **8**, 18 (2006).

[19] Chaves, A. & Rinaldi, C. Interfacial stress balances in structured continua and free surface flows in ferrofluids. *Physics of Fluids* **26**, 042101 (2014).

[20] Rosensweig, R. E. *Ferrohydrodynamics* (Courier Corporation, 2013).

[21] Kropinski, M. C. A. An Efficient Numerical Method for Studying Interfacial Motion in Two-Dimensional Creeping Flows. *Journal of Computational Physics* **171**, 479–508 (2001).